Chapter 4

Nickel doped Lithium-vacant Layered $Li_yCr_{1-x}Ni_xO_2$: A Potentially Active Electrocatalyst for Oxygen Evolution Reaction

Chapter 4

Nickel doped Lithium-vacant Layered $Li_yCr_{1-x}Ni_xO_2$: A Potentially Active Electrocatalyst for Oxygen Evolution Reaction

4.1 Introduction

In recent years, there has been a lot of interest in layered $LiMO_2$ (where M = Ni, Co, Mn, Fe, Cr) and its analogue as possible OER catalysts. The cathodes $LiCo_{1-x}O_2$ and $LiNi_{1-x}O_2$ of a Li-ion battery have been observed to evolve oxygen at $x > 0.55$ and $x > 0.8$, respectively, due to the pinning of the Co^{3+}/Co^{4+} and Ni^{3+}/Ni^{4+} redox energies at the top of the O(2*p*) bands [1, 2], suggesting that strong overlapping of the surface oxygen to the redox active cation is a prerequisite for good OER activity. The interplay of layered crystal structure and mixing of O(2*p*) band in M(3*d*) levels via the tuning of oxidation state of transition metal ions by varying the Li-content in the structure is one of the interesting ways to improve the OER activity of the catalyst. This may help for correlating the material characteristics with electrocatalytic activity [3-5]. Li^+ ions can be extracted via chemical and electrochemical methods from layered oxides. An increase in OER mass activity has been seen through the electrochemical delithiation of layered $LiCoO_2$ to $Li_{0.5}CoO_2$ in a non-aqueous electrolyte via the pinning of $Co^{3+/4+}$(3*d*) energy with the top of the O^{2-}(2*p*) band [4]. Compared to the synthesized sample, the chemical delithiation of layered $LiCoO_2$ with NO_2BF_4 produced $Li_{0.64}CoO_2$, $Li_{0.34}CoO_2$, and $Li_{0.09}CoO_2$ with similar mass activities but lower specific activities [5]. Further, the effect of ex situ chemical and in situ electrochemical delithiation on the OER activity of $LiNi_{0.7}Co_{0.3}O_2$ and $LiNi_{0.7}Co_{0.2}Fe_{0.1}O_2$ were also studied by Augustyn *et al* [6]. Over the past few years, doping of different metal ions (M = Co, Fe, Mn) in Ni-rich layered $LiNi_{1-x}M_xO_2$ oxides can be used to improve the catalytic activity by varying the Ni content, nature of the transition-metal dopant, lithium content, and degree of cation ordering between Li and Ni/ M [7]. Solution combustion

synthesized Al-doped lithium nickel oxides ($LiNi_{1-x}Al_xO_2$) were shown to suppress the mixing of Ni^{2+} in the Li^+ layer but obtain a higher concentration of Ni^{3+} played a crucial role in achieving excellent and stable OER activity by the tuning of Ni^{3+}/Ni^{4+} redox [8].

Recently, layered $LiCrO_2$ have garnered much interest, because of its multi-electron transfer process during the electrochemical reaction [9, 10]. In our earlier report, we noticed that doping of Fe in $LiCrO_2$ can result in better and stable OER activity due to the presence of Cr^{6+} ions at Li-interstitial sites and creating a thermodynamically stable dumbbell defect containing layered structure that facilitates the formation of −Cr−O−OH, which is crucial for O_2 evolution in alkaline media and higher stability of the catalyst [11].

Furthermore, redox potential of lithium transition metal oxides can also be tuned by introducing the foreign metal substituents in the lattice. We believe that metal substituents (X^{n+}) with higher electronegativity than parent metal (M^{m+}) can shift redox potential towards the more positive side by increasing ionicity of M-O bond via the inductive effect, resulting in a greater overlap between M(3*d*) and O(2*p*) orbital and thereby can improve the OER kinetics [12]. To confirm our hypothesis, we conducted the substitution of a more electronegative Ni^{3+} ion in $LiCrO_2$ that can significantly increase the ionicity of counterpart Cr-O bond through the inductive effect and shifting the redox potential more positively which can result in a greater overlap between Cr(3*d*) and O(2*p*) orbital and thus enhancing the OER activity of catalyst. In this work, we systematically studied the OER activity of layered $Li_yCr_{1-x}Ni_xO_2$ ($y \leq 1$, $0 \leq x \leq 0.2$) with different Ni doping amounts synthesized via a conventional solid-state reaction as well as solution combustion method. The XRD and Rietveld refinement result shows that the intensity ratio of (003)/(104) peaks decreases upon Ni-substitution demonstrating a decrease in layered ordering due to the formation of partial Li-vacancy and cation mixing in the structure (i.e., a part of Li-vacancies occupied by some of the Cr^{6+} ions). Ni-substitution can substantially induce the oxidation of Cr^{3+} to Cr^{6+} ion through inductive effect by enhancing the ionicity of

Cr-O bond which then occupies the Li-interstitial site creating dumbbell defect in layered $Li_yCr_{1-x}Ni_xO_2$ lattice, confirmed with the XPS and FTIR results and can contribute to superior OER activity of Ni doped $LiCrO_2$ catalyst. The electrochemical results shows that the combustion synthesized LCNO-10 (c) sample with the nominal composition of $LiCr_{0.9}Ni_{0.1}O_2$ exhibits highest activity with a Tafel slope of 63 mV dec^{-1} and an overpotential of 277 mV at a current density of 10 mA cm^{-2}. The activity of solution combustion synthesized $LiCr_{0.9}Ni_{0.1}O_2$ remarkably competes with the performance of RuO_2 (336 mV at 10 mA cm^{-2}) and showed superior or comparable OER activity to the other best-known OER catalysts such as α-MnO_2 [13], $Ba_{0.5}Sr_{0.5}Co_{0.8}Fe_{0.2}O_{3-\delta}$ (BSCF) [14], and $LaNiO_3$ [15].

4.2 Experimental section

4.2.1 Materials synthesis

$LiCrO_2$ and Ni-doped $LiCrO_2$ were synthesized following two methods: solid-state reaction and solution-combustion. The precursor compounds were purchased from Sigma Aldrich in their highest purity form available. For the solid-state reaction, the precursor compounds such as Li_2CO_3, Cr_2O_3 and $Ni(CH_3COO)_2.4H_2O$ were ground for half an hour in their stoichiometric ratio with an agate mortar-pestle set. The sample mixture was first fired at 550 ℃ for 6 h and then heated at 800 ℃ for 30 h in O_2 atmosphere with an intermediate grinding. For solution-combustion synthesis, an aqueous solution containing a stoichiometric amount of Li_2CO_3, $Cr(NO_3)_3.9H_2O$ and $Ni(NO_3)_2.6H_2O$ and $Co(NH_2)_2$ (urea as fuel) was mixed in a glass beaker and heated rapidly at 400-450 ℃ in a hood furnace. The solution then boils, froths, and, burns at a high flame temperature releasing gases in the process and yielding the desired product. The obtained product is then finally calcined at 800 ℃ for 12 h to get rid of residual carbon and to obtain a crystalline phase. The solid-state synthesized samples were denoted as LCNO-0(s), LCNO-5(s), LCNO-10 (s), LCNO-15(s), and LCNO-20(s) and the combustion synthesized samples were denoted as LCNO-0(c), LCNO-5(c), LCNO-10(c), LCNO-15(c), and LCNO-

20(c) for $LiCrO_2$, $LiCr_{0.95}Ni_{0.05}O_2$, $LiCr_{0.9}Ni_{0.1}O_2$, $LiCr_{0.85}Ni_{0.15}O_2$, $LiCr_{0.8}Ni_{0.2}O_2$, respectively. Further, $LiNi_{0.9}Cr_{0.1}O_2$ were also synthesized by solution combustion method using urea as a fuel and denoted as LNCO-10(c). The commercial RuO_2 was obtained from Sigma Aldrich (99%), which was tested as benchmark catalyst in the paper.

4.3 Results and discussion

4.3.1 XRD analysis and Rietveld refinement

Figure 4.1(a, b) shows the XRD pattern of all the solid-state and combustion synthesized $Li_yCr_{1-x}Ni_xO_2$ ($y \leq 1$, $0 \leq x \leq 0.2$) samples, denoted as LCNO(s) and LCNO(c), respectively. All the samples have a characteristic hexagonal α-$NaFeO_2$-type structure with the space group of $R\bar{3}m$, and the diffraction lines are well indexed with the standard rhombohedral phase of $LiCrO_2$ (JCPDS No. 00-024-0600). For both the combustion and solid-state method, up to 20% of Ni could be substituted for Cr in $LiCrO_2$, before any impurity peaks were detected in the XRD pattern. The splitting in the diffraction line of (006)/(012) and (108)/(110) doublets indicate a well-ordered layered structure for all the samples [16]. A decrease in the intensity ratio of (003) to (104) peaks, $I_{(003)}/I_{(104)}$, which is a measure of the degree of cation intermixing in the layered structure, with increasing Ni concentration in $LiCrO_2$ lattice was observed. A lower value of $I_{(003)}/I_{(104)}$ corresponds to a higher degree of cation intermixing [17]. The calculated $I_{(003)}/I_{(104)}$ values for all the solid-state and combustion synthesized samples are listed in **Table 4.1**, and also shown in **Figure 4.1(a, b)**. As can be seen, the intensity ratio of (003)/(104) peaks decreases significantly more in the case of LCNO(s) than in the case of LCNO(c), indicating that the degree of cation intermixing in the case of solid-state synthesized samples is higher than that of the combustion synthesized samples. This clearly demonstrates that the Ni substitution results in a better ordering of Li and Cr/Ni layer in the combustion synthesized LCNO(c) samples compared to the solid-state synthesized LCNO(s) samples.

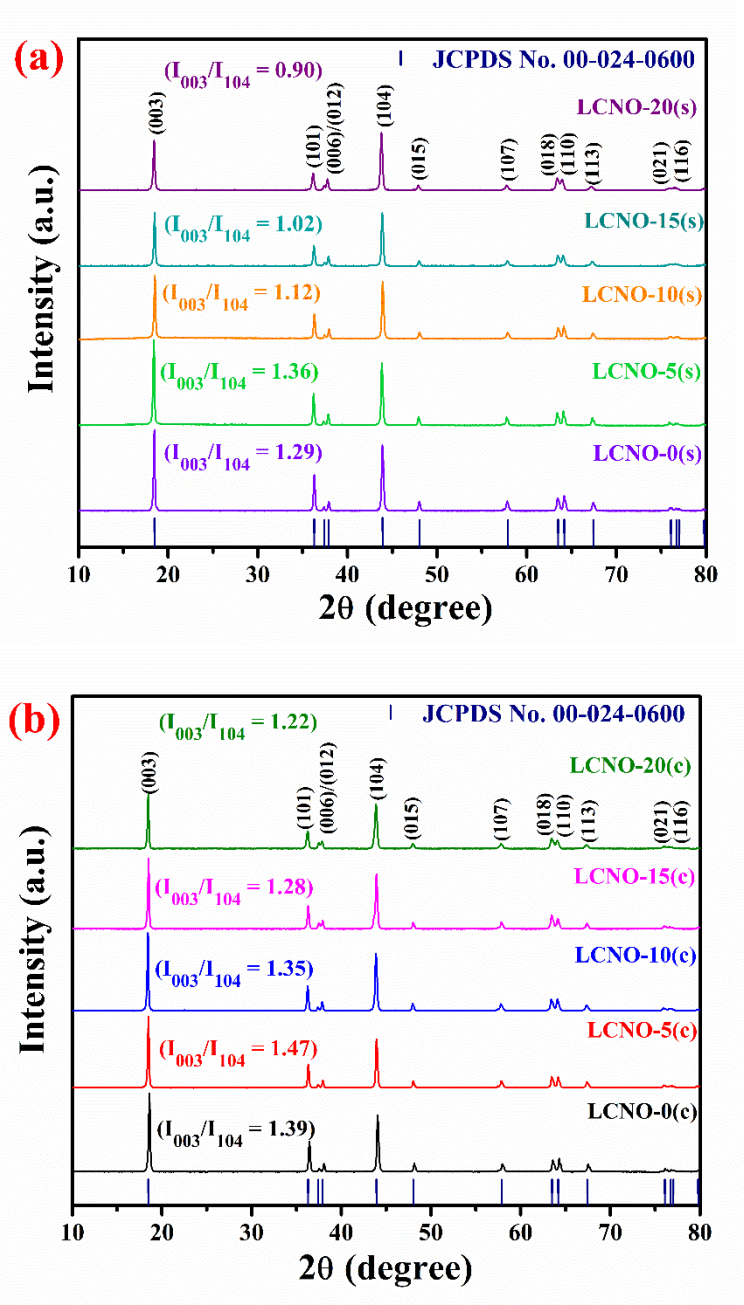

Figure 4.1 Powder XRD pattern of $Li_yCr_{1-x}Ni_xO_2$ ($y \leq 1$, $0 \leq x \leq 0.2$). **(a)** solid-state and **(b)** solution combustion synthesized samples.

As we know, combustion synthesized samples are less crystalline than solid-state samples, the degree of crystallinity was calculated of all the synthesized samples from the XRD patterns. For LCNO-10(c) and LCNO-20(c) samples, the degree of crystallinity (%) is found to be 66% and 61%, which is lesser than for LCNO-10(s)-77% and LCNO-20(s)-68%. The degree of crystallinity and cation-intermixing can significantly contribute to alter the OER activity of

catalysts. Rietveld refinement of XRD patterns was performed using FULLPROF suite software, in order to explain the effect of Ni-substitution in combustion synthesized LCNO(c) as well as solid-state synthesized LCNO(s) samples. Assuming a perfectly ordered α-$NaFeO_2$ type structure, the structures were first refined using Pseudo-Voigt as the peak profile function and $R\bar{3}m$ space group, where Cr^{3+}/Ni^{3+} ions occupy the 3*a* site (0, 0, 0), Li^+ ions occupy the 3*b* site (0, 0, 0.5), and O^{2-} ions occupy the 6*c* site (0, 0, Z_{ox}), (Z_{ox} = 0.24–0.25). Further, the isotropic thermal parameters (*B*) were allowed to vary while fixing the site occupancies in the subsequent step. The computations produced negative values for the lithium isotropic thermal parameters, *B*(Li), indicating an excess of electronic density in the lithium site due to the presence of Cr/Ni ions in the Li-layer [18]. This clearly confirms that Li vacancies were created in the Li-layer and some of these vacancies are occupied by the Cr/Ni ions **(Table 4.1)**. **Figure 4.2(a, b)** represents the Rietveld refined XRD patterns of LCNO(s) and LCNO(c), respectively. **Table 4.1** listed all the Rietveld refinement results obtained for LCNO(s) and LCNO(c) samples. The lattice parameters obtained by Rietveld refinements show significant changes upon Ni substitution revealing that the Ni is successfully incorporated in the $LiCrO_2$ lattice. From the refinement results it is obsrved that the a_{hex} parameter has slightly increased while the c_{hex} parameter has decreased upon increasing the Ni concentration in the $LiCrO_2$ lattice. A similar tendency in the lattice variation, (i.e., larger $a_{hex.}$ and shorter $c_{hex.}$ parameter) was observed for both LCNO(c) and LCNO(s) samples, which is in accordance with the Vegard's law [19]. This lattice variation can be explained by using the crystal lattice of $LiNiO_2$ (*a* = 2.878 0Å, *c* = 14.19 Å, $R\bar{3}m$ [20]) which shows a smaller $a_{hex.}$ and $c_{hex.}$ values than those of $LiCrO_2$ (*a* = 2.902 Å, *c* = 14.44 Å, $R\bar{3}m$ [21]). Concerning the a_{hex} parameter, it is important to consider the difference in ionic radii of Li^+, Cr^{3+}, Ni^{3+} and Ni^{2+} (r_{Li^+} = 0.74 Å, $r_{Cr^{3+}}$ = 0.615 Å, $r_{Ni^{3+}}$ = 0.56 Å (LS), $r_{Ni^{2+}}$ = 0.69 Å) [22] and as it was expected, the expansion of a_{hex} parameter is considerably due to the presence of larger Ni^{2+} ion in the lattice, indicating the partial intermixing of Ni-ion in the

Li-layer. On the other hand, when it comes to the c_{hex} parameter, one must consider separately the slab thickness (CrO_2 layer, S_{CrO_2}) and the interslab thickness (LiO_2 layer, I_{LiO_2}) that can vary in opposite directions upon cationic substitution [18]. As observed, with the shrinkage of c_{hex} parameter, the interslab thickness (I_{LiO_2}) decreases and the slab thickness (S_{CrO_2}) increases upon Ni-substitution in both combustion and solid-state compounds.

Table 4.1 Structural parameters obtained from Rietveld refinement of $Li_yCr_{1-x}Ni_xO_2$ ($y \leq 1$, $0 \leq x \leq 0.2$) synthesized by combustion and solid-state method.

	Samples	a_{hex} (Å)	c_{hex} (Å)	V_{hex} (Å^3)	z_{ox}	$S_{(CrO2)}$ (Å)[a]	$I_{(LiO2)}$ (Å)[b]	$B_{(Li)}$ Å^2	χ^2	R_{wp}	I_{003}/I_{104}
Solid-state method	**LCNO-0(s)**	2.9005	14.4308	105.14	0.2449	2.55	2.26	-0.31	2.03	22.5	1.29
	LCNO-5(s)	2.9015	14.4283	105.17	0.2445	2.56	2.25	-0.95	2.05	10.5	1.36
	LCNO-10(s)	2.9041	14.4250	105.35	0.2435	2.59	2.22	-1.65	2.15	14.2	1.12
	LCNO-15(s)	2.9067	14.4213	105.54	0.2429	2.61	2.19	-2.09	1.99	12.3	1.02
	LCNO-20(s)	2.9097	14.4117	105.66	0.2419	2.63	2.17	-2.36	2.01	13.5	0.90
Combustion method	**LCNO-0(c)**	2.9016	14.4348	105.25	0.2455	2.53	2.28	-0.91	2.35	23.2	1.39
	LCNO-5(c)	2.9024	14.4252	105.25	0.2447	2.56	2.25	-2.33	2.17	13.6	1.47
	LCNO-10(c)	2.9033	14.4223	105.29	0.2433	2.60	2.21	-3.47	2.11	12.5	1.35
	LCNO-15(c)	2.9045	14.4195	105.30	0.2422	2.63	2.17	-3.39	2.23	17.2	1.28
	LCNO-20(c)	2.9055	14.4036	105.36	0.2411	2.66	2.14	-2.43	2.13	14.3	1.22

Note:

[a] **Slab thickness: [$S_{(CrO2)} = 2\ [(1/3 - z_{ox})]\ c_{hex.}$]**

[b] **Interslab space thickness: [$I_{(LiO2)} = (c_{hex.}/3) - S_{(CrO2)}$]**

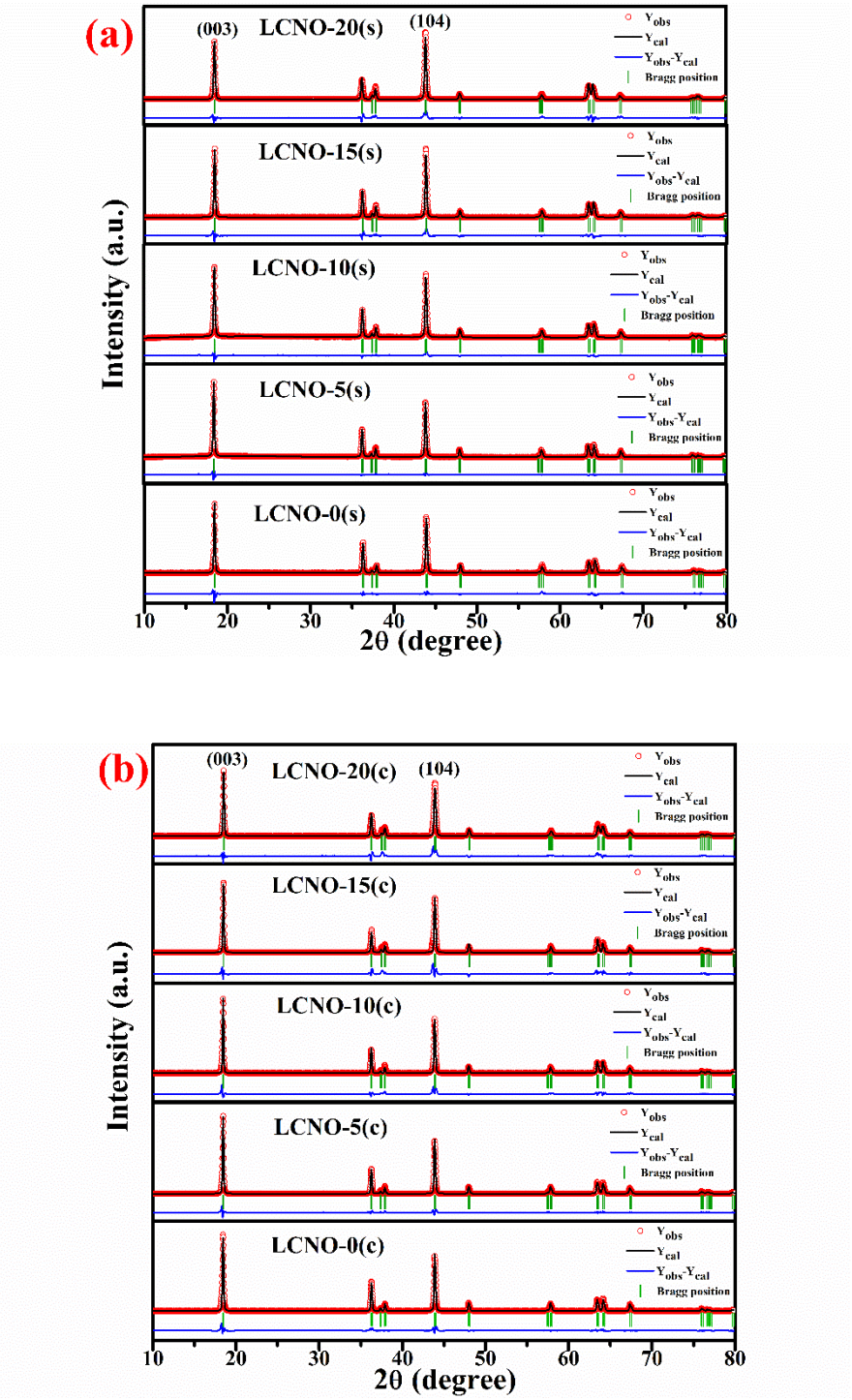

Figure 4.2 Rietveld refined powder XRD patterns of $Li_yCr_{1-x}Ni_xO_2$ ($y \leq 1$, $0 \leq x \leq 0.2$). **(a)** solid- state and **(b)** solution combustion synthesized samples.

When the system is Li-deficient, the repulsion between neighbouring CrO_2 layers increases (i.e., interslab thickness, I_{LiO_2} increases) which will become the source of instability in the system. As Cr/Ni ions migrates into Li-layers, and function as a link of CrO_2 layers, the bonding

between Cr/Ni ions at Li-site and O in CrO_2 layer causes the interslab thickness (I_{LiO_2}) to decrease, lowering the system's overall energy, and allowing the Cr/Ni antisites in Li-layer to stabilize the system in Li-deficient sites [10]. The presence of more electronegative Ni^{3+} ion in the Cr-layer (the electronegativity value of Ni^{3+} is ~1.695 and $Cr^{3+}$is ~1.587) [23], induces the formation of highly covalent Ni-O bond in the lattice by increasing effective charge on Cr ion (i.e., Cr^{6+}) and making the neighbouring Cr-O and Li-O bonds more ionic. Consequently, Ni substitution induces the Cr^{6+} ions to partially occupy the interstitial site of Li-layer creating dumbbell defect in the $Li_yCr_{1-x}Ni_xO_2$ and thereby stabilizing the layered structure of the system with partial Li-deficiency and cation mixing (Cr/Ni antisites in Li layer). Moreover, it was demonstrated that the combustion samples have smaller lattice parameter than the solid-state samples. This lattice contraction is attributed to the lower percentage of Ni^{2+}(in 6-fold CN = 0.69 Å) present in the combustion-synthesized samples, that also suggests that combustion compounds are more ordered with lesser intermixing of Ni^{2+} ion into the Li-layer, compare to the solid-state compounds. Reduced Ni^{2+} ion intermixing along with high concentration of Cr6+ ion in Li-layer (as further elucidated in XPS analysis) and a low degree of crystallinity can significantly contribute to enhance the OER activity of combustion samples.

The crystal structure of $Li_yCr_{1-x}Ni_xO_2$ ($y \leq 1$, $0 \leq x \leq 0.2$) having layered rhombohedral structure with $R\bar{3}m$ space group is shown in the **Figure 4.3(a-c)**. The perfect $R\bar{3}m$ structure **(Figure 4.3a)** and partial lithium deficient structure **(Figure 4.3b)** of $LiCrO_2$ shows that transition metal sites (3*a*) and lithium sites (3*b*) are separated into two layers without any cation intermixing. **Figure 4.3c** presents layered $Li_yCr_{1-x}Ni_xO_2$ structure having Li-vacancies along with the partial mixing of Cr/Ni-ion in the Li-layer. The Li-O and Cr-O layer corresponds to the (003) plane presenting the layered structure and (104) plane corresponds to Li-O-Cr layer presenting both the layered and the cubic structure. As can be seen from XRD, upon Ni substitution, the intensity of (003) plane decreases, which suggests decrease in layered ordering and creation of

Li^+ vacancy in this plane. On the other hand, the intensity of (104) plane increases which is Li-O-Cr plane. This increase in (104) plane signifies that Ni is mostly substituted in this catalytically active plane, resulting from the partial Cr/Ni mixing in Li-O-Cr layer.

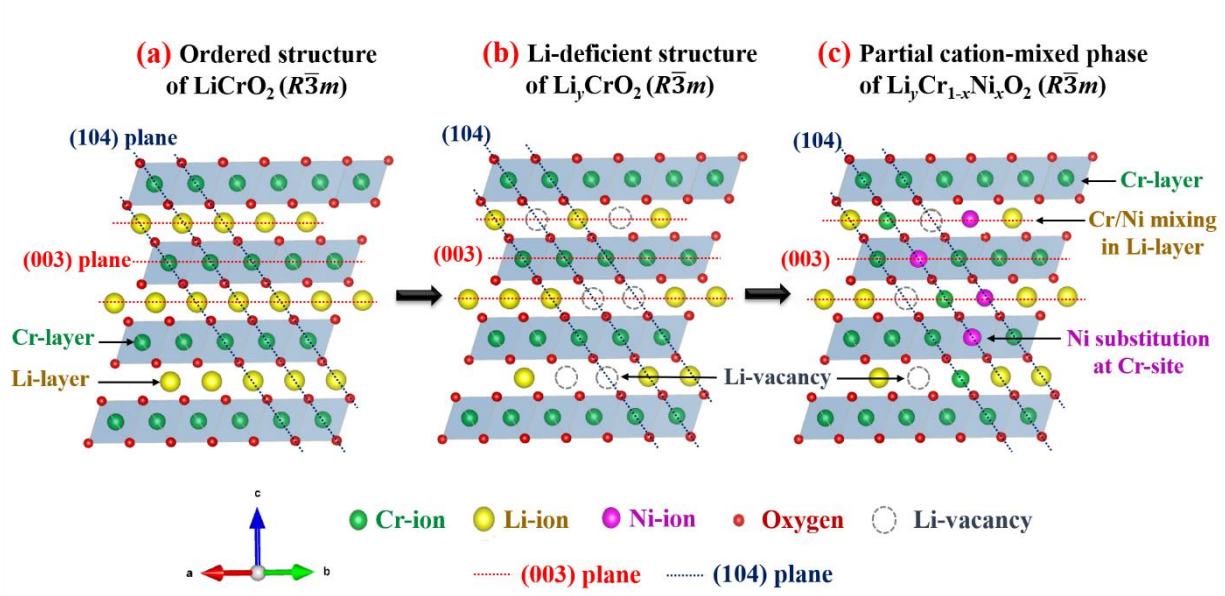

Figure 4.3 Schematic illustration of structural transformation in layered $Li_yCr_{1-x}Ni_xO_2$.

4.3.2 XPS and ICP analysis

XPS measurements were performed to investigate the chemical state of transition metals (Cr and Ni) present in the synthesized samples. **Figure 4.4(a, b)** represents the Cr(2*p*) core-level spectra for solid-state LCNO(s) and combustion LCNO(c) samples, respectively. The Cr(2*p*) spectra consist of two doublet binding energies i.e., Cr $2p_{3/2}$ and Cr $2p_{1/2}$ which was deconvoluted into two chemical states i.e., Cr^{3+} (blue line) and Cr^{6+} (red line) [24]. The respective binding energies and relative concentrations of Cr(2*p*) spectra for the samples synthesized by either method is summarized in **Table 4.2**. As observed, for the samples synthesized by either method, the Cr $2p_{3/2}$ and Cr $2p_{1/2}$ peaks were shifted to the higher binding energies with the Ni substitution, supporting the presence of high concentration of Cr^{6+} ion in the lattice. For combustion samples, the concentration of Cr^{6+} ion is much higher than the solid-

state samples, indicating that there is more mixing of Cr^{6+} ion in Li-interstitial site which results in a dumbbell defect in the lattice.

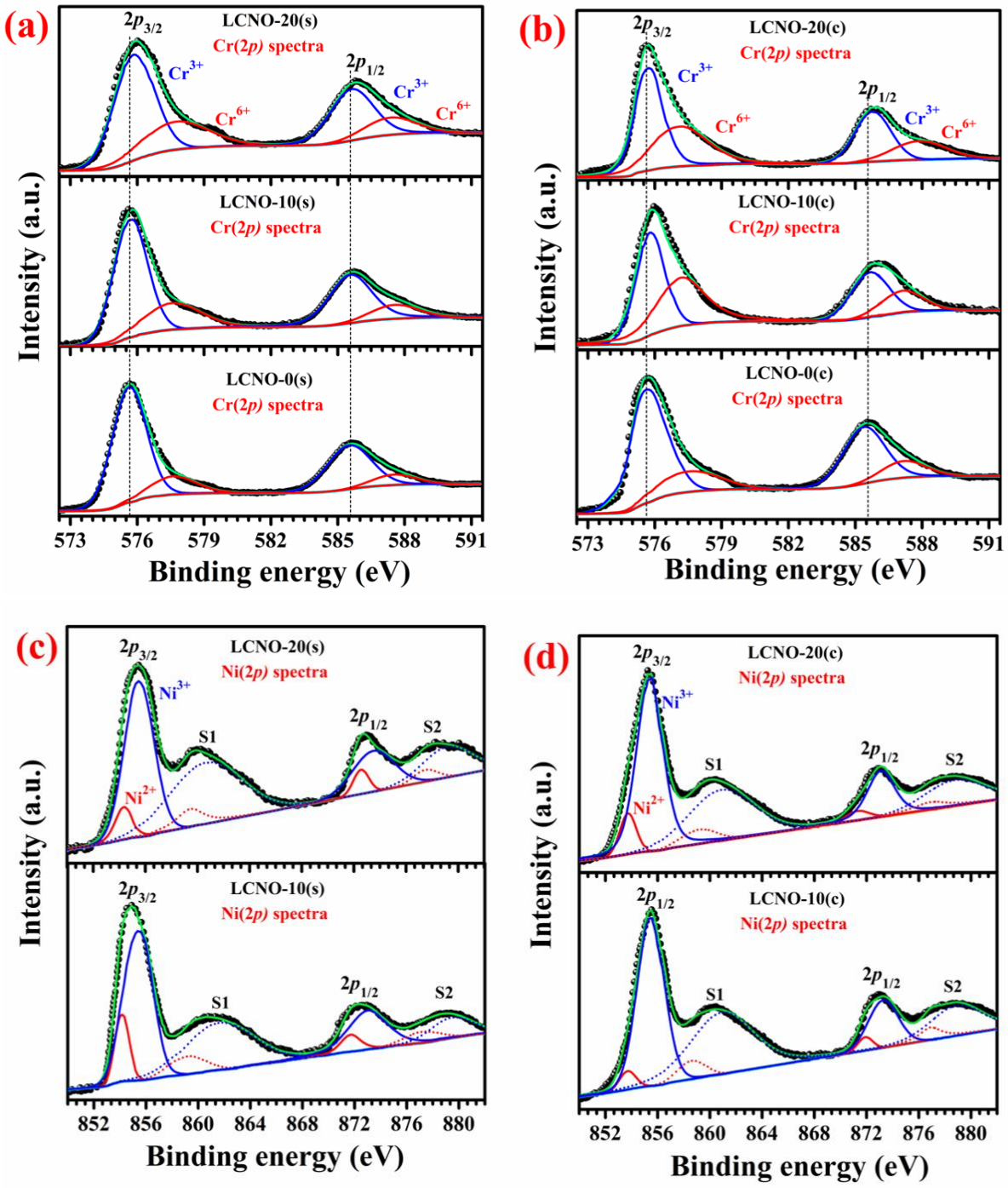

Figure 4.4 Core level XPS spectra of **(a, b)** Cr 2p (blue and red line colors correspond to Cr^{3+} and Cr^{6+}chemical states, respectively) and **(c, d)** Ni 2p (red and blue line colors correspond to $Ni^{2+}$and Ni^{3+}chemical states, respectively).

Further, the core-level spectra of Ni(2*p*) for doped LCNO(s) and LCNO(c) samples are shown in the **Figure 4.4(b, c)**, respectively. The spectra consist of two doublets, i.e., Ni $2p_{1/2}$ and Ni $2p_{3/2}$ along with two respective satellite peaks (i.e., S1 and S2) that could be fitted with two chemical states, i.e., major Ni^{3+} (blue line) and minor Ni^{2+} (red line) [8]. The corresponding binding energies and relative concentration are summarized in **Table 4.3**, which shows that both the combustion and solid-state samples require more than one peak for Ni 2*p* doublets indicating the mixed valence states for Ni (+3 and +2). The presence of minor Ni^{2+} component confirms the partial mixing of Ni^{2+} ion in the Li-layer. In case of combustion samples, the concentration of Ni^{2+} is very low, confirming lower mixing of Ni ion in the Li-layer along with the high concentration of Cr^{6+} ion in the lattice, compare to the solid-state ones. As a result of the presence of more electronegative Ni^{3+} ion in $LiCrO_2$ lattice, the effective charge on Cr ions is increased due the inductive effect of the neighbouring Ni^{3+} which in turn will increase the ionicity of the Cr-O bond (supported by the refinement results).

Table 4.2 XPS deconvoluted peak positions and % composition in Cr(2p) spectra for $Li_yCr_{1-x}Ni_xO_2$ ($y \leq 1$, $0 \leq x \leq 0.2$) synthesized by combustion and solid-state method.

Samples			**Binding energy (eV)**		**Relative concentration (%)**
			$2p_{3/2}$	**$2p_{1/2}$**	
Solid state method	**LCNO-0(s)**	Cr^{3+}	575.3	585.4	89
		Cr^{6+}	577.5	587.4	11
	LCNO-10(s)	Cr^{3+}	575.7	585.6	81
		Cr^{6+}	577.6	587.6	19
	LCNO-20(s)	Cr^{3+}	575.8	585.8	74
		Cr^{6+}	577.7	587.7	26
Combustion method	**LCNO-0(c)**	Cr^{3+}	575.6	585.3	86
		Cr^{6+}	577.5	587.2	14
	LCNO-10(c)	Cr^{3+}	575.9	585.7	67
		Cr^{6+}	577.4	587.3	33
	LCNO-20(c)	Cr^{3+}	575.7	585.5	71
		Cr^{6+}	577.4	587.4	29

Table 4.3 XPS deconvoluted peak positions and % composition in Ni(2p) spectra for $Li_yCr_{1-x}Ni_xO_2$ ($y \leq 1$, $0 \leq x \leq 0.2$) synthesized by combustion and solid-state method.

Samples			Binding energy (eV)				Relative concentration (%)
			$2p_{3/2}$	$2p_{1/2}$	S1	S2	
Solid state method	LCNO-10(s)	Ni^{3+}	855.3	873.1	861.4	878.9	76
		Ni^{2+}	853.6	871.4	859.3	877.0	24
	LCNO-20(s)	Ni^{3+}	855.4	873.3	861.1	879.0	81
		Ni^{2+}	853.8	871.3	859.4	877.1	19
Combustion method	LCNO-10(c)	Ni^{3+}	855.5	873.3	861.2	879.2	90
		Ni^{2+}	853.9	871.6	859.2	877.1	10
	LCNO-20(c)	Ni^{3+}	855.4	873.4	861.1	879.1	85
		Ni^{2+}	853.7	871.5	859.3	877.2	15

In addition, the relative concentration of Cr, Ni, and Li in the samples was investigated by the ICP analysis. The nominal (desired) and actual composition (obtained from the ICP-MS analysis) of all the combustion and solid-state synthesized $Li_yCr_{1-x}Ni_xO_2$ ($0 \leq x \leq 0.2$) samples are listed in **Table 4.4**. The results clearly confirm presence of Li-vacancy in our synthesized samples due to the high temperature calcination.

Table 4.4 The nominal and ICP composition of $Li_yCr_{1-x}Ni_xO_2$ ($y \leq 1$, $0 \leq x \leq 0.2$) synthesized by combustion and solid-state method.

Samples		Nominal Composition	ICP composition
Combustion method	LCNO-0(c)	$LiCrO_2$	$Li_{0.77}CrO_2$
	LCNO-5(c)	$LiCr_{0.95}Ni_{0.05}O_2$	$Li_{0.80}Cr_{0.95}Ni_{0.05}O_2$
	LCNO-10(c)	$LiCr_{0.90}Ni_{0.10}O_2$	$Li_{0.70}Cr_{0.90}Ni_{0.10}O_2$
	LCNO-15(c)	$LiCr_{0.85}Ni_{0.15}O_2$	$Li_{0.78}Cr_{0.85}Ni_{0.15}O_2$
	LCNO-20(c)	$LiCr_{0.80}Ni_{0.2}O_2$	$Li_{0.75}Cr_{0.80}Ni_{0.2}O_2$
Solid-state method	LCNO-0(s)	$LiCrO_2$	$Li_{0.67}CrO_2$
	LCNO-5(s)	$LiCr_{0.95}Ni_{0.05}O_2$	$Li_{0.75}Cr_{0.95}Ni_{0.05}O_2$
	LCNO-10(s)	$LiCr_{0.90}Ni_{0.10}O_2$	$Li_{0.73}Cr_{0.90}Ni_{0.10}O_2$
	LCNO-15(s)	$LiCr_{0.85}Ni_{0.15}O_2$	$Li_{0.72}Cr_{0.85}Ni_{0.15}O_2$
	LCNO-20(s)	$LiCr_{0.80}Ni_{0.2}O_2$	$Li_{0.70}Cr_{0.80}Ni_{0.2}O_2$

4.3.3 Microstructural analysis

The surface morphology of synthesized samples was examined by scanning electron microscopy (SEM). **Figure 4.5(a, b)** represents the SEM image of combustion synthesized $LiCr_{0.9}Ni_{0.1}O_2$(c) and solid-state synthesized $LiCr_{0.8}Ni_{0.2}O_2$(s) samples, respectively. The materials exhibit quasi hexagonal structure with the particle size ranging from 100-350 nm. It was observed that the particles?? of combustion samples are smaller compare to the solid-state samples. The energy dispersive X-ray spectroscopy analysis was used to determine the elemental composition of prepared material. **Figure 4.5(c, d)** and **(e, f)** shows the elemental mapping and EDS spectra of LCNO-10(c) and LCNO-20(s) samples, respectively, indicating the presence of Cr, Ni and O in the synthesized material. The EDS spectra confirms that the obtained elemental composition (Cr: Ni = 0.90:0.10) in LCNO-10(c) and (Cr: Ni = 0.81: 0.19) in LCNO-20(s) is same as the nominal composition taken for the synthesis. Li cannot be detected in the sample using SEM-EDS because of the low excitation energy of the Li element.

The microstructure of the synthesized LCNO-10(c) and LCNO-20(s) samples were further confirmed with the HR-TEM analysis. The high-resolution TEM micrographs and selected area diffraction (SAED) pattern **(Figure 4.6a–f)** show the highly crystalline quasi-hexagonal particles existing in the synthesized material. The particles are roughly in range between 100-350 nm for both the combustion and solid-state samples, **(Figure 4.6a**, **b)**, which are consistent with the SEM results. The well-defined lattice fringes with a *d*-spacing of 4.78 Å for LCNO-10(c) and 4.76 Å for LCNO-20(s) **(Figure 4.6c, d)**, matched with the (003) plane of layered $LiCrO_2$ (space group $R\bar{3}m$), which is also confirmed through XRD. The selected area electron diffraction (SAED) pattern **(Figure 4.6e, f)** shows distinct ring-like pattern corresponding to the lattice planes of (003), (101), (006), (104), (015), (107), (018) and (110) that depict the

synthesized LCNO-10(c) and LCNO-20(s) samples are polycrystalline in nature with a typical quasi-hexagonal structure and space group $R\bar{3}m$.

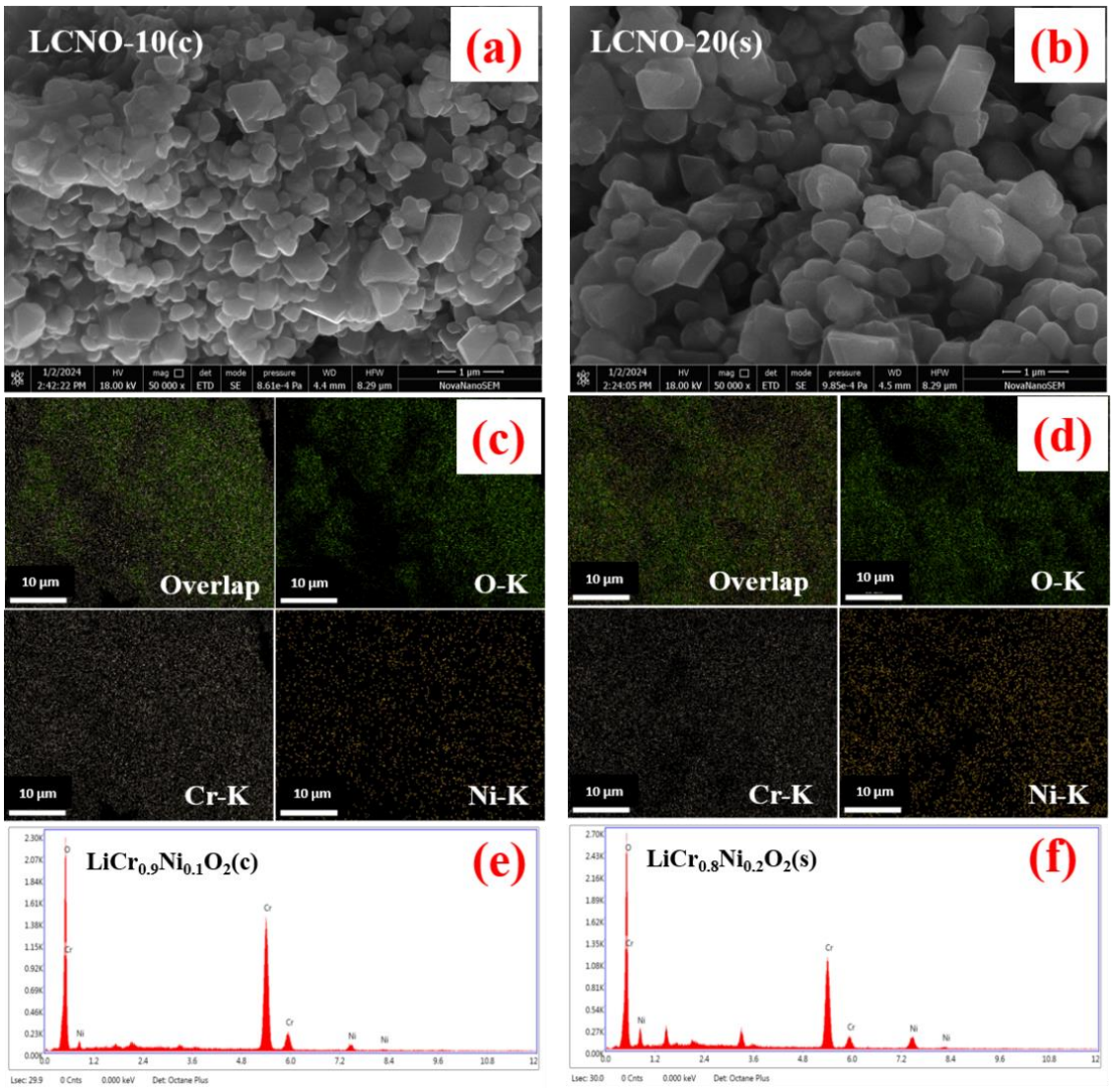

Figure 4.5 SEM micrograph of **(a)** LCNO-10(c) (scale bar: 1 µm with 50,000x magnification), **(b)** LCNO-20(s) (scale bar: 1 µm with 50,000x magnification), **(c, d)** elemental mapping of individual elements (O, Cr, and Ni) present in the LCNO-10(c) and LCNO-20(s) samples, respectively and **(e, f)** EDX spectrum of LCNO-10(c) and LCNO-20(s). Note: Li signals are absent in EDX analysis as EDX techniques are not capable of recording signals for the Li core level.

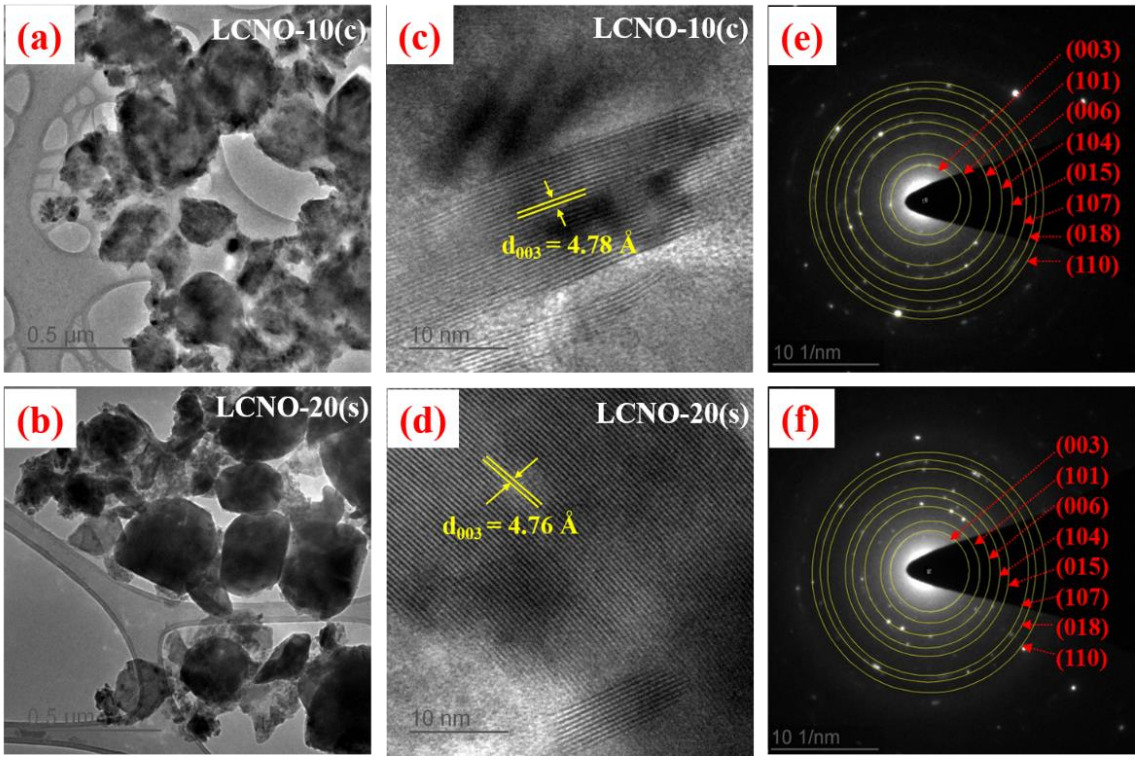

Figure 4.6 (a, b) Bright field TEM image, **(c, d)** HR-TEM with interplanar d-spacing of (003) plane and **(e, f)** SAED pattern of LCNO-10(c) and LCNO-20(s) samples, respectively.

4.3.4 FTIR analysis

The FT-IR spectroscopic data of $LiCr_{1-x}Ni_xO_2$ synthesized by combustion and solid-state method reveal the local structure of the oxide lattice created by LiO_6 and CrO_6/NiO_6 octahedra. The spectra were recorded in the range between 400–4000 cm^{-1} **(**see **Figure 4.7)**. The resonance frequencies of the alkali metal cations in the octahedral interstices (LiO_6) are in the frequency range of 200–400 cm^{-1} [25]. But due to instrumental limitations, FT-IR spectra for $LiCr_{1-x}Ni_xO_2$ could not be recorded below 400 cm^{-1}. Because of the inter-atomic vibrations, metal oxides generally exhibit absorption bands below 1000 cm^{-1}. The absorption bands appear in the region of 400–700 cm^{-1} is due to the stretching and bending vibration of Cr-O and Ni-O bonds present in CrO_2 layer. The strong peak in the region of 800-950 cm^{-1} is attributed to the CrO_4^{2-} vibration confirming the presence of Cr^{6+} ion [11, 26]. The peak ~1109 cm^{-1} is due to the Cr^{3+}-O-H

bending vibration. A very weak band ~1433 cm^{-1} confirms the presence of Ni-O bond in the lattice [27]. The absorption bands observed at 1650 and 3390 cm^{-1} is due to the O-H bending and O-H stretching vibrations. The FT-IR observation clearly demonstrates that successful formation of layered $Li_yCr_{1-x}Ni_xO_2$ structure and the presence of Cr^{6+} ion in Li- interstitial sites creating dumbbell defect in the $Li_yCr_{1-x}Ni_xO_2$ lattice.

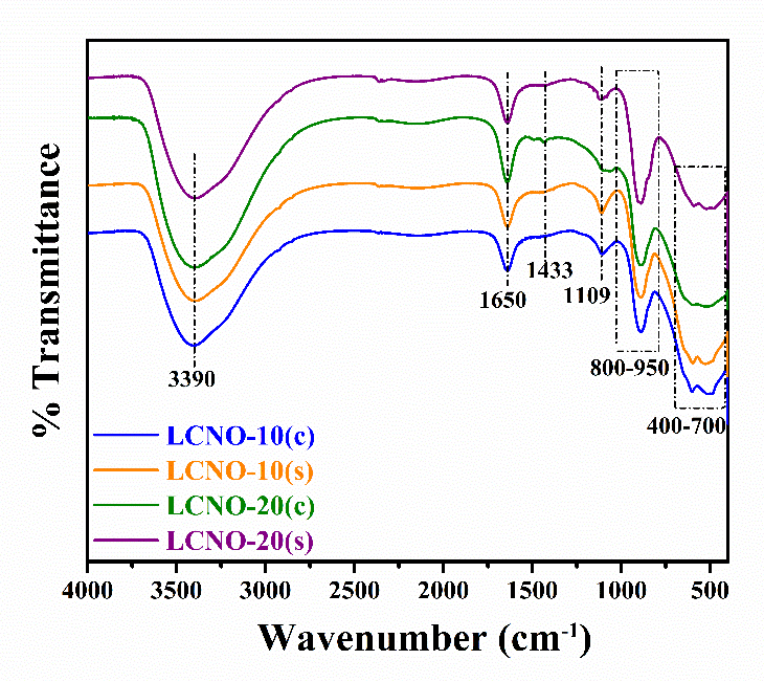

Figure 4.7 FTIR spectra of solid-state and combustion synthesized LCNO samples.

4.3.5 Electrochemical studies

4.3.5.1 OER performances of synthesized catalysts

The OER activity of all the solid-state synthesized $Li_yCr_{1-x}Ni_xO_2$(s): $y \leq 1$, $0 \leq x \leq 0.2$ (designated as LCNO(s)) samples were displayed in **Figure 4.8a**. The LSV curve shows that the current densities were enhanced with increasing Ni concentration in $LiCrO_2$. The $Li_yCr_{0.8}Ni_{0.2}O_2$(s) composition (designated as LCNO-20(s)) displayed highest activity among the solid-state synthesized LCNO(s) samples. **Figure 4.8b** depicts the bar diagram of the overpotential values at 10 mA cm^{-2} current density which shows that LCNO-0(s), LCNO-5(s),

LCNO-10(s), LCNO-15(s) and LCNO-20(s) demand overpotential values of 374, 348, 350, 335 and 326 mV, respectively. On the other hand, the OER activity of all the combustion synthesized $Li_yCr_{1-x}Ni_xO_2$(c): $y \leq 1$, $0 \leq x \leq 0.2$ (designated as LCNO(c)) samples are given in **Figure 4.8c**.

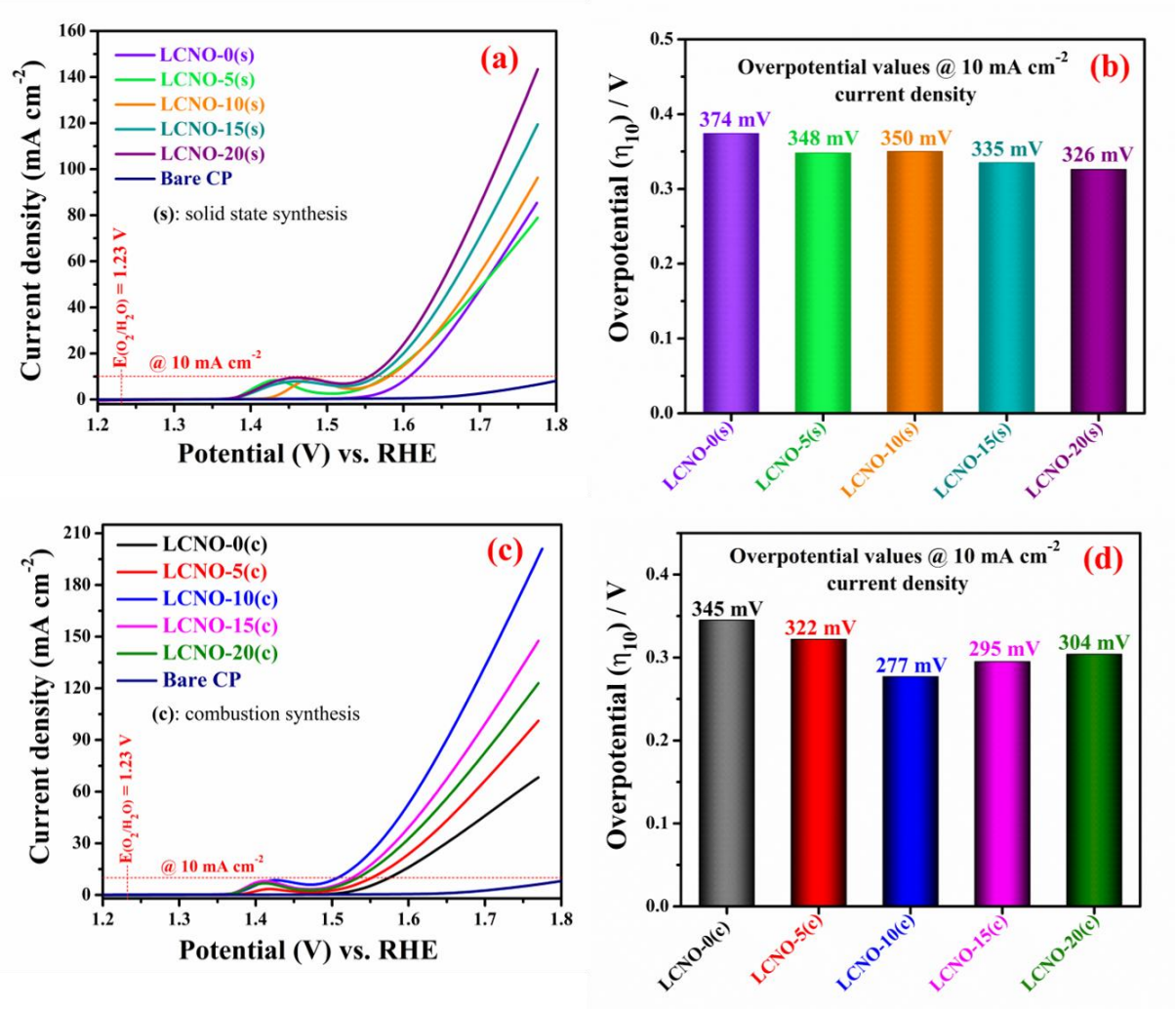

Figure 4.8 OER performance of LCNO ($Li_yCr_{1-x}Ni_xO_2$; $y \leq 1$, $0 \leq x \leq 0.2$) synthesized by combustion and solid-state method **(a, c)** Linear sweep voltammograms taken at a scan rate of 5 mV s^{-1} in 1 M KOH and **(b, d)** Overpotentials (error values ±2 mV) at a current density of 10 mA cm^{-2}.

All the combustion synthesized samples showed remarkably highest activity in terms of reduced onset potential (i.e., the minimum potential required to start a reaction at the electrode surface) and higher current densities compared to the solid-state synthesized samples. The OER

activity of $Li_yCr_{0.9}Ni_{0.1}O_2$(c) composition (designated as LCNO-10(c)) is highest among all the combustion synthesized samples. **Figure 4.8d** represents the bar diagram of the overpotential values at 10 mA cm^{-2} current density which shows that LCNO-10(c) can deliver 10 mA cm^{-2} current density at a very low overpotential of 277 mV, which is significantly lower than 295, 304, 322 and 345 mV for LCNO-15(c) LCNO-20(c), LCNO-5(c), and LCNO-0(c), respectively.

4.3.5.2 OER kinetic analysis

The electrocatalytic reaction kinetics of these OER catalysts were examined by Tafel plots extracted from LSV curves. The polarization curves were replotted as overpotential (η) versus the logarithm of current density (log |j|) to obtain Tafel slopes (in **Figure 4.9a**). The slope value obtained for LCNO-0(s), LCNO-5(s), LCNO-10(s), LCNO-15(s), and LCNO-20(s) are approximately 79, 103, 95, 97 and 90 mV dec^{-1}, respectively. The Tafel slopes of all the combustion synthesized samples, in **Figure 4.9b**, for LCNO-0(c), LCNO-5(c), LCNO-10(c), LCNO-15(c) and LCNO-20(c) are approximately 101, 93, 65, 73 and 81 mV dec^{-1}, respectively. The lowest Tafel slope of LCNO-10(c) (65 mV dec^{-1}) indicates its much faster reaction kinetics among all the combustion synthesized LCNO(c) as well as solid-state synthesized LCNO(s) samples. Moreover, EIS measurements were performed at a potential of 1.55 V vs. RHE to investigate the charge-transfer kinetics at the electrode/electrolyte interface. **Figure 4.9(c, d)** represents the Nyquist plot of all the solid-state synthesized LCNO(s) and combustion synthesized LCNO(c) samples, which can be fitted using equivalent circuit composed of electrolyte resistance (R_s), a constant phase element (CPE), and a charge transfer resistance (R_{ct}). The semicircle loop in Nyquist plot represents the charge-transfer resistance (R_{ct}), which is an important parameter to investigate the OER kinetics of catalysts. The fitted R_{ct} values for all the solid-state synthesized and combustion synthesized samples are listed in **Table 4.5**. The highly active LCNO-10(c) possesses a lower R_{ct} value of 6.64 Ω at 1.55 V vs.

RHE, suggesting enhanced interfacial charge transfer kinetics among all the combustion synthesized and solid-state synthesized catalysts.

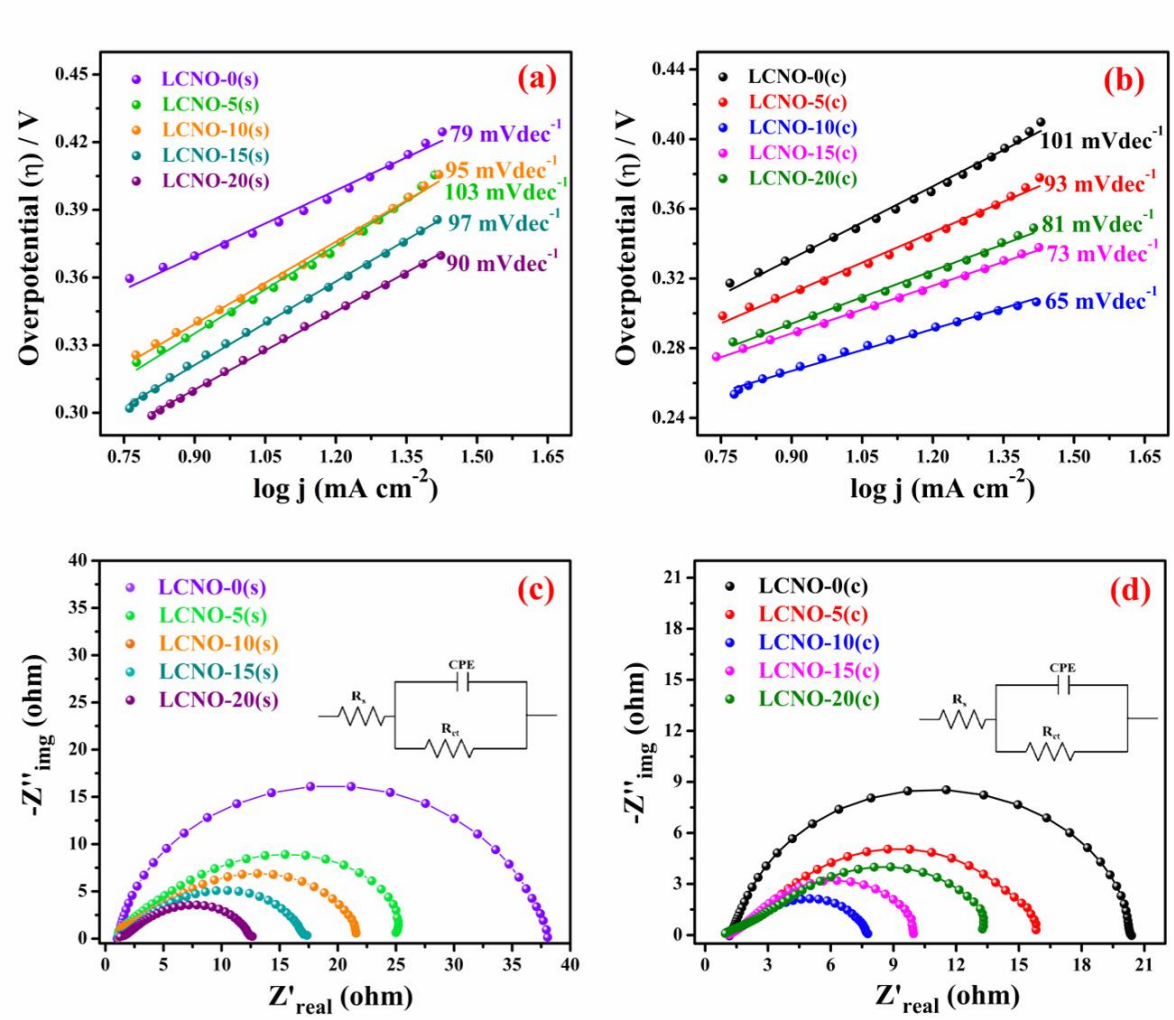

Figure 4.9 Kinetic analysis **(a, b)** Tafel slope and **(c, d)** EIS recorded at 1.55 V vs. RHE of LCNOs ($Li_yCr_{1-x}Ni_xO_2$; $y \leq 1$, $0 \leq x \leq 0.2$) synthesized by combustion and solid-state method, respectively.

Table 4.5 The fitted R_{ct} values from the Nyquist plot for $Li_yCr_{1-x}Ni_xO_2$ ($y \leq 1$, $0 \leq x \leq 0.2$) catalysts synthesized by combustion and solid-state method.

Solid-state synthesized samples (s)	R_{ct} (Ω)	Combustion synthesized samples (c)	R_{ct} (Ω)
LCNO-0(s)	37.03(±0.01)	LCNO-0(c)	19.25(±0.02)
LCNO-5(s)	23.66(±0.04)	LCNO-5(c)	14.65(±0.02)
LCNO-10(s)	20.45(±0.02)	LCNO-10(c)	6.64(±0.01)
LCNO-15(s)	16.24(±0.01)	LCNO-15(c)	8.85(±0.01)
LCNO-20(s)	11.36(±0.01)	LCNO-20(c)	12.29(±0.01)

4.3.5.3 Comparative OER study

In the present study, commercial RuO_2 (as reference catalyst) was tested under the same experimental condition and its activity is compared with synthesized oxide catalysts. From the **Figure 4.10a**, solid-state synthesized LCNO-20(s) markedly approaches the performance of benchmark catalyst RuO_2, and the combustion synthesized LCNO-10(c) shows much higher activity compared to the commercial RuO_2 **(Figure 4.10a)**. RuO_2 requires 336 mV overpotential to reach a current density of 10 mA cm^{-2} (similar to Ananthraj's report) [28], whereas, LCNO-10(c) requires 277 mV overpotential to achieve the same current density. The overpotential values to achieve 10mA cm^{-2} current density is represented in the form of bar diagram, **Figure 4.10b**, which follows the order: LCNO-10(c) (η_{10} = 277 mV) < LCNO-20(c) (η_{10} = 304 mV) < LCNO-20(s) (η_{10} = 326 mV) < RuO_2 (η_{10} = 336 mV) < LCNO-10(s) (η_{10} = 350 mV). Besides, the Tafel plot and Nyquist plot were also shown in **Figure 4.10(c, d)**, separately. The Tafel slope and R_{ct} values of synthesized catalysts along with commercial RuO_2 (as a benchmark catalyst) are listed in **Table 4.6**. The lower value of the Tafel slope (63 mV dec^{-1}) and charge transfer resistance (R_{ct} = 6.64 Ω) of LCNO-10(c), clearly demonstrates its superior OER activity among all the synthesized catalyst and reference RuO_2.

Table 4.6 Tafel slope and R_{ct} values of synthesized catalysts along with commercial RuO_2 (as a benchmark catalyst).

Catalysts	**Tafel slope (mV dec^{-1})**	**R_{ct} (Ω)**
RuO_2	83	17.33(±0.01)
LCNO-10(c)	65	6.64(±0.01)
LCNO-20(c)	81	12.29(±0.01)
LCNO-10(s)	95	20.45(±0.02)
LCNO-20(s)	90	11.36(±0.01)

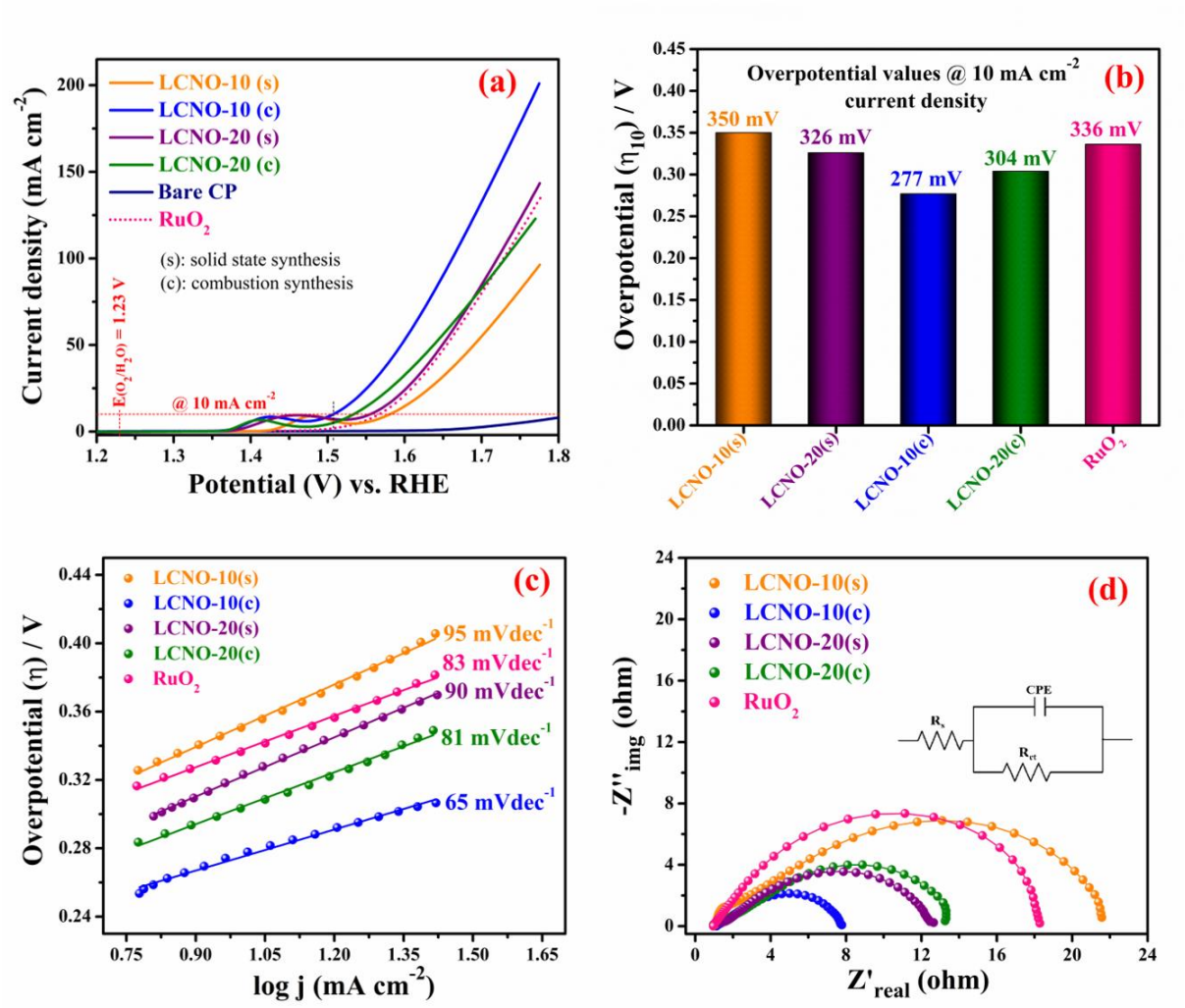

Figure 4.10 Comparison of OER performance of LCNO-10(c), LCNO-20(c), LCNO-10(s), and LCNO-20(s) with commercial RuO_2, **(a)** Linear sweep voltammograms recorded at 5 mV s^{-1} in 1 M KOH, **(b)** Overpotentials at a current density of 10 mA cm^{-2}, **(c)** Tafel plots and **(d)** EIS measurement at an applied potential of 1.5 V vs. RHE.

4.3.5.4 Cyclic voltammograms for redox reaction

The LSV curves **(Figure 4.8a, c)** shows that an anodic peak is present in the pre-OER region of all the combustion synthesized and solid-sate synthesized catalysts. These pre-OER faradaic behavior depicts the in-situ activation of catalysts that was attributed to the oxidation of Cr^{3+} to Cr^{6+} (a three-electron transfer reaction with single redox) coupled with the electrochemical delithiation at higher oxidation potentials, making the structure more Li-deficient [9-11, 29]. To facilitate the understanding of these pre-OER anodic peaks, CV measurements were

performed in the potential region between 1.1–1.6 V vs. RHE, as illustrated in **Figure 4.11(a, b)**. All the combustion synthesized and solid-state synthesized catalysts exhibit a reversible redox peak between the potential range of 1.3–1.5 V vs. RHE. The substitution of Ni in $LiCrO_2$ lattice induces a positive shift in the redox peak. This shift can be attributed to the contribution of Ni^{2+}/Ni^{3+} redox coupled with the Cr^{3+}/Cr^{6+} redox during the electrocatalytic process. In order to illustrate that the peaks arise in the CV measurements are not due to the diffusion effect, we also examined the catalyst activity under rotating disk electrode (RDE) where the CV curve clearly exhibit a redox peak corresponds to the $Cr^{6+/3+}$ redox couple which facilitates the electron transfer process during the OER (**Figure 4.11c)**. This data supports the idea that it is not diffusion-related surface adsorption. Furthermore, according to the earlier reports, the OER activity of metal oxides can be related to the potential of redox processes, $[M^{n+}\text{-}OH_{ad}]/[Mn^{+1}\text{-}O_{ad}]$, prior to the onset of OER, [6, 7]. A positive shift in the redox potential for the oxidation of surface metal ions is associated with the improved OER kinetics [12]. Further, it was suggested that metal-ion (X^{n+}) substituents with greater electronegativity and lower pK_a of $[X(H_2O)_m]^{n+}$ is shown to positively shift the formal redox potential of parent metal in transition metal complexes and (hydr-)oxides, which can be explained by inductive effect. Metal substituents (X^{n+}) with higher electronegativity compared to parent metal (M^{m+}) can pull electrons from M^{m+} and lower the energy of antibonding states that would result in a decrease of electron energy associated with the redox of metal-ligand (M-O) bonds by shifting the electron density from parent metal (M) to ligand forming a more ionic M-O bond in transition metal complexes. This can lead to an optimized binding of the reaction intermediates on the surface in rate-limiting steps [12]. In the present study, as already mentioned, Ni substitution can substantially shift the redox potential to a more positive side **(Figure 4.11a, b)**. This is because of the inductive effect due to the substitution of highly electronegative Ni^{3+} ion in $LiCrO_2$ lattice (the electronegativity value of Ni^{3+} is ~1.695 and Cr^{3+} is ~1.587) [22]. The more

electronegative Ni^{3+} ion have higher affinity to electrons than Cr^{3+} ion, which can induce the formation of highly covalent Ni-O bond in $LiCr_{1-x}Ni_xO_2$. The highly covalent of Ni-O bond makes the counterpart Cr-O and Li-O bonds more ionic (by increasing the effective charge on chromium, i.e., Cr^{6+}), that would lead to decrease the redox energy of filled antibonding states of Cr-O bond (resulting in greater overlap between Cr(3*d*) and O(2*p*) orbital), and shift the redox potential to a more positive side, thereby leading to an improved OER kinetics of catalysts.

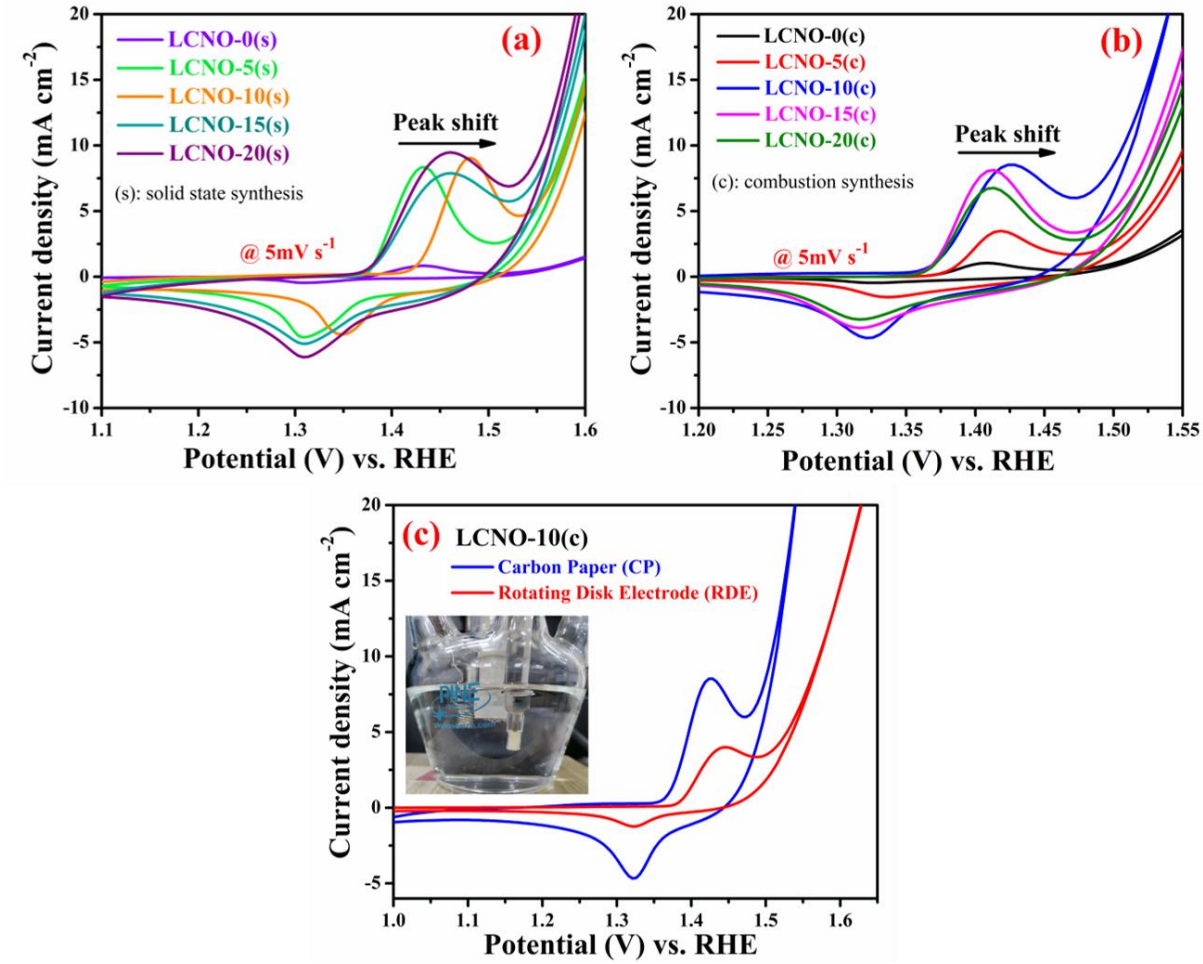

Figure 4.11 Cyclic voltammograms (CV) recorded at a scan rate of 5 mV s^{-1} in 1 M KOH, **(a)** solid-state synthesized, **(b)** combustion synthesized $Li_yCr_{1-x}Ni_xO_2$ samples with different Ni concentrations, respectively; demonstrating the effect of Ni-substitution on the pre-OER redox behaviour of the catalysts and **(c)** CV measurement of LCNO-10(c) using a rotating disk electrode (RDE) in 1 M KOH at a rotation speed of 1600 rpm.

Furthermore, as can be seen in **Figure 4.11a**, the anodic peak potential of the solid-state synthesized samples is shifted more positively along with the increased onset potential for OER, in contrast to the combustion synthesized samples which show a positive shift in both the anodic and cathodic peak along with the reduced onset potential for OER **(Figure 4.11b)**. This observation is also confirmed with the XPS results, as Ni^{2+} concentration is higher in case of solid-state synthesized catalyst, the contribution of Ni^{2+}/Ni^{3+} redox is higher, resulting the more positive shifting of anodic peak along with the increased onset for OER, compare to the combustion synthesized samples. Nonetheless, among all the solid-state and combustion synthesized catalysts, LCNO-10(c) showed superior OER activity because of its low OER onset and positive redox potential.

4.3.5.5 Electrochemically active surface area (ECSA)

In addition, for ascertaining the possible reason behind the high activity of the combustion synthesized catalysts, the electrochemical active surface (ECSA) area was determined by C_{dl} (double-layer capacitance) methods in non-faradic potential regions of 0.9–0.1 V vs. Ag/AgCl at scan rates of 50, 70, 100, 120, 140, 160 mV s^{-1}, and the observed cyclic voltammetry (CV) outcomes are given in **Figure 4.12a-g**. The C_{dl} values were calculated by plotting the current density differences (ΔJ/2) against scan rates where the slope represents C_{dl} **(Figure 4.13a)**. Electrochemical active surface area (ECSA) of the catalysts were calculated by using the following formula:

$$ECSA = \frac{C_{dl}}{C_s} \tag{4.1}$$

Where C_s is the specific capacitance of the material per unit area under identical electrolyte conditions. C_s = 0.040 mF cm^{-2} in 1.0 M KOH based on reported values [30]. The observed C_{dl} and the calculated ECSA values of the catalysts were given in the **Table 4.7**.

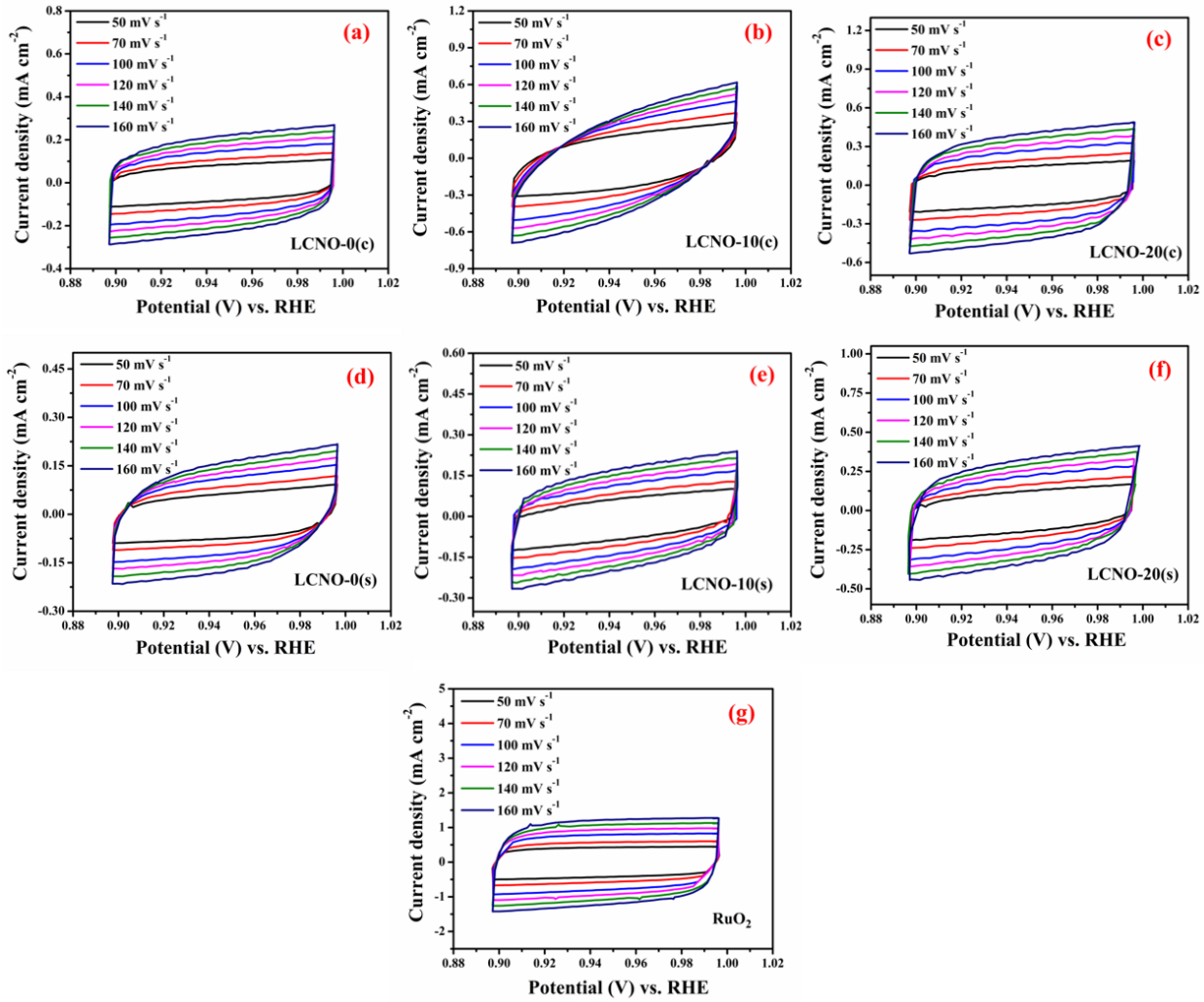

Figure 4.12 Determination of double layer capacitance (C_{dl}) of different LCNOs synthesized by solid-state and combustion method, and commercial RuO_2. **(a-g)** CV measurements in a non-faradic current region (0.9-1.0 V vs. RHE) at scan rates of 50, 100, 120, 140 and 160 mV s^{-1}in 1 M KOH electrolyte.

As we can see, LCNO-10(c) exhibits a C_{dl} value of 3.2 mF cm^{-2} with the calculated ECSA of 80 cm^2 mg^{-1}, which is higher among all the combustion and solid-state synthesized LCNO catalysts, but much lesser than that of RuO_2 (C_{dl} = 7.9 mF cm^{-2} and ECSA = 197.5 cm^2 mg^{-1}). **Figure 4.13b** represents the OER current density of different catalysts achieved at 350 mV overpotential against ECSA. It is observed, from the **Figure 4.13b**, that the current density of LCNO-10(c) is higher than that of all the combustion and solid-state synthesized LCNO catalysts and the commercial RuO_2, implying the largest intrinsic activity of LCNO-10(c).

Hence, it is concluded that LCNO-10(c) with higher ECSA facilitates higher reactant adsorption for OER.

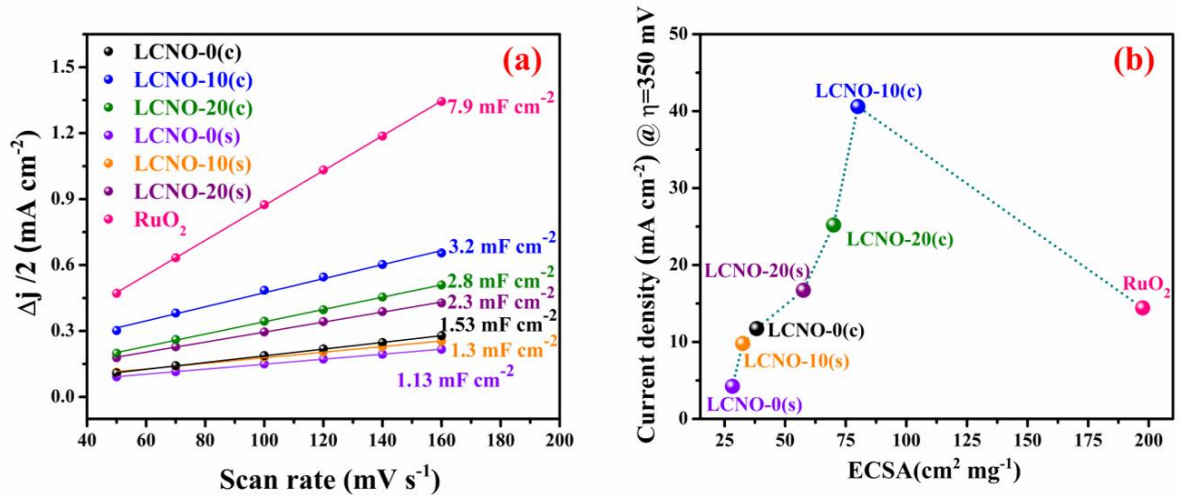

Figure 4.13 (a) Plots of capacitive current density differences (Δj) vs. scan rate (C_{dl} slope) and **(b)** plot of current density (mA cm^{-2}) of different catalysts achieved at 350 mV overpotential vs. ECSA (cm^2 mg^{-1}).

Table 4.7 Calculated C_{dl} and ECSA values for $Li_yCr_{1-x}Ni_xO_2$ ($y \leq 1$, $0 \leq x \leq 0.2$) catalysts synthesized by combustion and solid-state method along with commercial RuO_2 (as a benchmark catalyst).

Catalyst	C_{dl} (mF cm^{-2})	ECSA (cm^2 mg^{-1})
LCNO-0(c)	1.53	38.25
LCNO-10(c)	3.2	80
LCNO-20(c)	2.8	70
LCNO-0(s)	1.13	28.25
LCNO-10(s)	1.3	32.5
LCNO-20(s)	2.3	57.5
RuO_2	7.9	197.5

4.3.5.6 Long-term stability test

Despite the catalytic activity, long-term stability is an important parameter to govern the practical applicability of the electrocatalysts. The stability of the LCNO-10(c) and LCNO-20(s) was examined by performing chronoamperometry (CA) and cyclic voltammetry (CV)

measurements. **Figure 4.14(a, b)** represents the CA plot of LCNO-10(c) and LCNO-20(s) samples measured at 1.5 and 1.56 V vs. RHE, respectively for 12 h. As depicted in **Figure 4.14a**, LCNO-10(c) initially exhibit a steady current density of 10 mA cm^{-2} that was slightly increases over the span of 12 h period, indicating a good current retention of LCNO-10(c) even after 12 h. Conversely, LCNO-20(s) show an initial current density of 10 mA cm^{-2} that was slightly decreases over the span of 12 h period **(Figure 4.14b)**. In addition, the inset of **Figure 4.14(a, b)** shows the LSV curves of LCNO-10(c) and LCNO-20(s) samples at the 1st, 100th, 500th, and 1000th cycle scans during the continuous cyclic voltammetry (CV) measurements. In contrast to LCNO-20(s), which exhibits a slightly higher potential associated with a decreased current density after 1000 cycles, LCNO-10(c) exhibits a small reduction in potential, suggesting its good stability even after 1000 cycles. This clearly indicates that the best-performing OER catalyst, i.e., the combustion synthesized LCNO-10(c) shows an excellent stability in a highly alkaline 1 M aqueous KOH electrolyte.

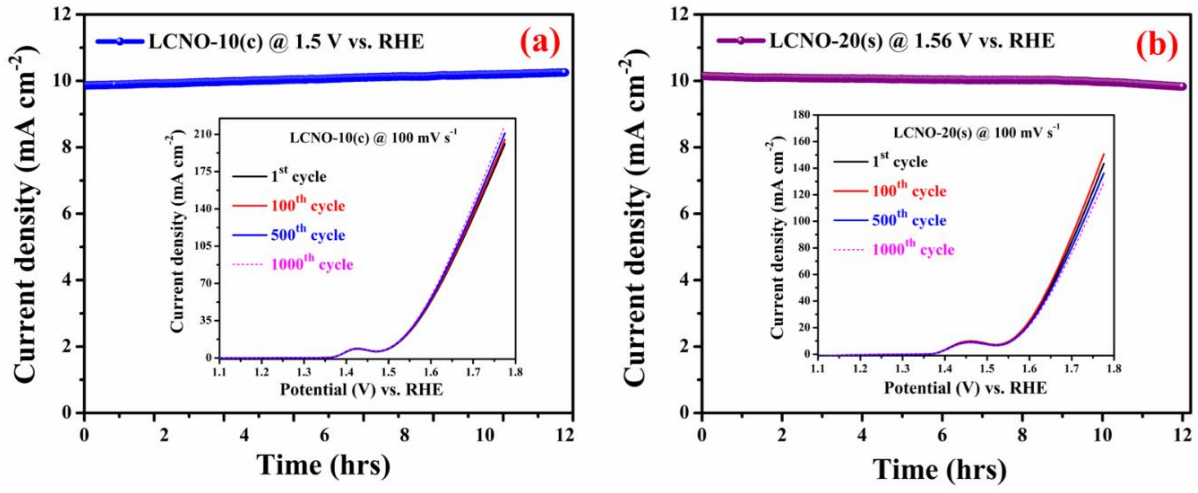

Figure 4.14. Long-term stability test **(a)** chronoamperogram of LCNO-10(c) at an applied potential of 1.5 V vs. RHE for 12 hrs, **(b)** chronoamperogram of LCNO-20(s) at an applied potential of 1.56 V vs. RHE for 12 hrs; inset of **(a, b)** shows the linear sweep voltammograms for the 1st, 100th, 500th and 1000th cycle at a scan rate of 100 mV s^{-1}.

4.3.6 Post-OER characterizations

After the long-term stability test, the post-OER characterizations were carried out to see the effect of electrochemical cycling on the microstructure of combustion and solid-state synthesized catalysts i.e., LCNO-10(c) and LCNO-20(s).

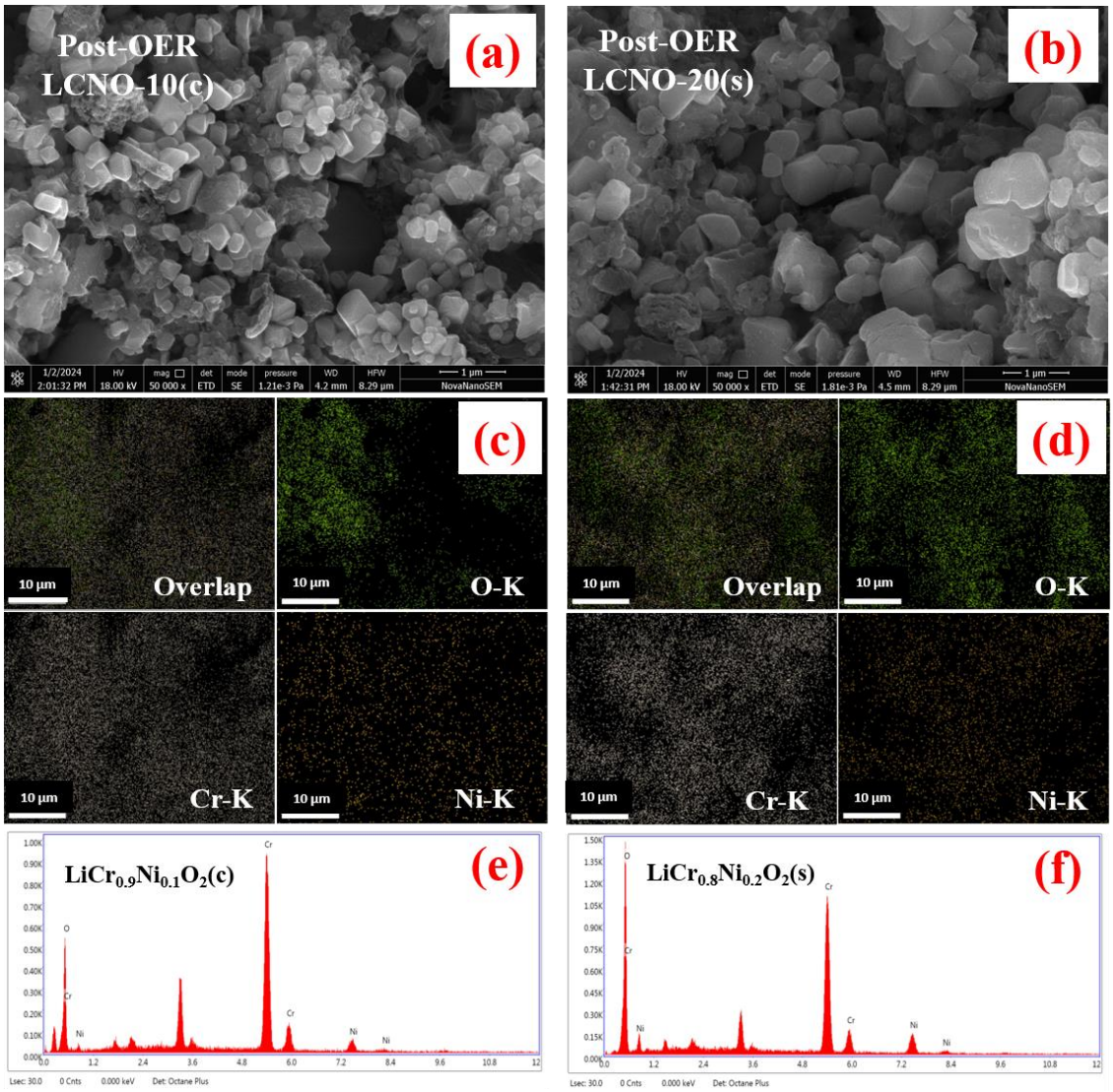

Figure 4.15 Post OER SEM micrographs of **(a)** LCNO-10(c) (scale bar: 1µm with 50,000x magnification), **(b)** LCNO-20(s) (scale bar: 1µm with 50,000x magnification), **(c, d)** corresponding elemental mapping and **(e, f)** EDX spectrum confirming the presence of O, Cr, and Ni in the LCNO-10(c) and LCNO-20(s) electrodes, respectively. Note: Li signals are absent in EDX analysis as EDX techniques are not capable of recording signals for the Li core level.

The post-OER SEM images of LCNO-10(c) and LCNO-20(s) electrodes reveal that the morphology is maintained even after long-term anodic cycling **(Figure 4.15a, b)**. In addition, the elemental mapping and EDS spectra confirms the existence of Cr, Ni, and O elements in the structure **(Figure 4.15c−f)**. Furthermore, the post-OER XRD analysis of the LCNO-10(c) and LCNO-20(s) samples, **(Figure 4.16)** reveal the layered α-$NaFeO_2$ structure ($R\bar{3}m$) is maintained even after the long-term stability test. Other than the carbon paper peak, no discernible peak shifting in the diffraction pattern has been identified. However, the relative intensity ratio of (003) to (104) peak is remarkably decreased from 1.35 to 0.73 and 0.9 to 0.55 for LCNO-10(c) and LCNO-20(s) samples respectively, indicating that degree of cation-mixing is significantly increases during the electrocatalytic reaction. Some of the Li^+ ion has been extracted during the electrocatalytic process that enables the Cr/Ni ions to migrate from the Cr-layer to the Li-layer, and making the layered structure more disordered. This results clearly confirms that the in-situ activation of the catalyst is attributed to the oxidation of $Cr^{3+}$to Cr^{6+} along with Ni^{2+}/Ni^{3+} redox during the electrocatalytic process.

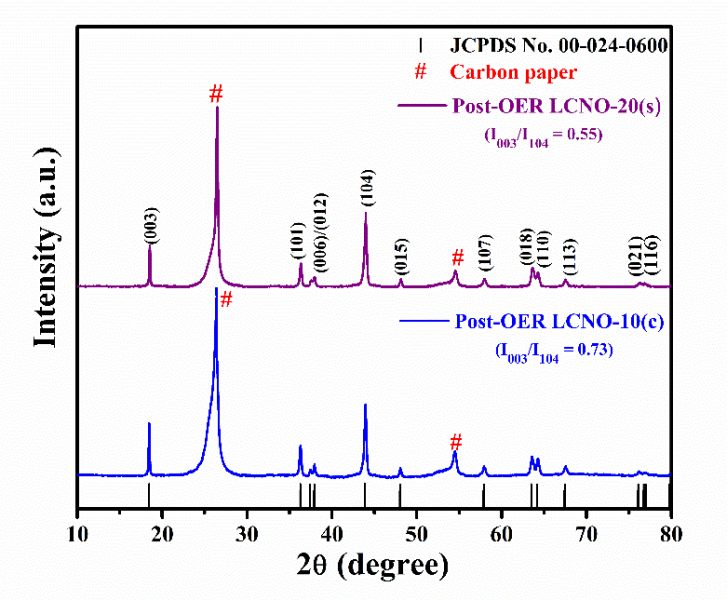

Figure 4.16. Post OER XRD pattern of LCNO-10(c) and LCNO-20(s) electrodes.

4.4 Conclusion

For both the combustion and solid-state method, up to 20% of Ni could be substituted for Cr in $LiCrO_2$, before any impurity peaks were detected in the XRD pattern. All the samples have a characteristic hexagonal α-$NaFeO_2$-type structure with the space group of $R\bar{3}m$ and the diffraction peaks are well indexed with the standard rhombohedral phase of $LiCrO_2$ (JCPDS No. 00-024-0600). The XRD and Rietveld refinement result shows that the intensity ratio of (003)/(104) peaks decreases upon Ni-substitution demonstrating a decrease in layered ordering due to the formation of partial Li-vacancy and cation mixing in the structure (i.e., a part of Li-vacancies occupied by some of the Cr^{6+} ions). Ni-substitution can substantially induce the oxidation of Cr^{3+} to Cr^{6+} ion which then occupies the Li-interstitial site creating dumbbell defect in layered $Li_yCr_{1-x}Ni_xO_2$ lattice and can contribute to superior OER activity of Ni-doped $LaCrO_2$ catalyst. The FT-IR studies confirm the successful formation of layered $Li_yCr_{1-x}Ni_xO_2$ structure and, demonstrates the presence of Cr^{6+} ion in Li- interstitial sites creating dumbbell defect in the $Li_yCr_{1-x}Ni_xO_2$ lattice. The binding energies of Ni (2*p*) and Cr(2*p*), obtained from XPS studies confirm that the presence of more electronegative Ni^{3+} ion in $LiCrO_2$ lattice which can significantly increase the effective charge on Cr ions, which in turn, increases the ionicity of the Cr-O bond due to the high covalency of Ni-O bond through the inductive effect (also supported by the Rietveld refinement results). The electrochemical results confirm that the combustion synthesized LCNO-10(c) sample with the nominal composition of $LiCr_{0.9}Ni_{0.1}O_2$ exhibits the highest activity with a Tafel slope of 63 mV dec^{-1} and an overpotential of 277 mV at a current density of 10 mA cm^{-2}. The activity of solution combustion synthesized $LiCr_{0.9}Ni_{0.1}O_2$ remarkably competes with the performance of RuO_2 (336 mV at 10 mA cm^{-2}) and showed superior or comparable OER activity to the other best-known OER catalysts such as α-MnO_2, $Ba_{0.5}Sr_{0.5}Co_{0.8}Fe_{0.2}O_{3-\delta}$ (BSCF), and $LaNiO_3$.

4.5 References

1. Chebiam, R.V., Kannan, A.M., Prado, F. and Manthiram, A., 2001. Comparison of the chemical stability of the high energy density cathodes of lithium-ion batteries. *Electrochemistry Communications*, *3*(11), pp.624-627.
2. Chebiam, R.V., Prado, F. and Manthiram, A., 2001. Soft Chemistry Synthesis and Characterization of Layered $Li_{1-x}Ni_{1-y}Co_yO_{2-\delta}$ ($0\leq x\leq 1$ and $0\leq y\leq 1$). *Chemistry of Materials*, *13*(9), pp.2951-2957.
3. Lu, Z., Wang, H., Kong, D., Yan, K., Hsu, P.C., Zheng, G., Yao, H., Liang, Z., Sun, X. and Cui, Y., 2014. Electrochemical tuning of layered lithium transition metal oxides for improvement of oxygen evolution reaction. *Nature Communications*, *5*(1), p.4345.
4. Maiyalagan, T., Jarvis, K.A., Therese, S., Ferreira, P.J. and Manthiram, A., 2014. Spinel-type lithium cobalt oxide as a bifunctional electrocatalyst for the oxygen evolution and oxygen reduction reactions. *Nature Communications*, *5*(1), p.3949.
5. Colligan, N., Augustyn, V. and Manthiram, A., 2015. Evidence of Localized Lithium Removal in Layered and Lithiated Spinel $Li_{1-x}CoO_2$ ($0\leq x\leq 0.9$) under Oxygen Evolution Reaction Conditions. *The Journal of Physical Chemistry C*, *119*(5), pp.2335-2340.
6. Augustyn, V. and Manthiram, A., 2015. Effects of chemical versus electrochemical delithiation on the oxygen evolution reaction activity of nickel-rich layered $LiMO_2$. *The Journal of Physical Chemistry Letters*, *6*(19), pp.3787-3791.
7. Augustyn, V., Therese, S., Turner, T.C. and Manthiram, A., 2015. Nickel-rich layered $LiNi_{1-x}M_xO_2$ (M=Mn, Fe, and Co) electrocatalysts with high oxygen evolution reaction activity. *Journal of Materials Chemistry A*, *3*(32), pp.16604-16612.
8. Gupta, A., Chemelewski, W.D., Buddie Mullins, C. and Goodenough, J.B., 2015. High-rate oxygen evolution reaction on Al-doped LiNiO2. *Advanced Materials*, *27*(39), pp.6063-6067.
9. Balasubramanian, M., McBreen, J., Davidson, I.J., Whitfield, P.S. and Kargina, I., 2002. In situ X-ray absorption study of a layered manganese-chromium oxide-based cathode material. *Journal of the Electrochemical Society*, *149*(2), p.A176.
10. Lyu, Y., Ben, L., Sun, Y., Tang, D., Xu, K., Gu, L., Xiao, R., Li, H., Chen, L. and Huang, X., 2015. Atomic insight into electrochemical inactivity of lithium chromate ($LiCrO_2$): Irreversible migration of chromium into lithium layers in surface regions. *Journal of Power Sources*, *273*, pp.1218-1225.

11. Soni, V., Mondal, R., Singh, A.N., Singh, P. and Gupta, A., 2023. Dumbbell Defect Containing Chromium-Rich Lithium-Vacant Layered $Li_yCr_{1-x}Fe_xO_2$ ($y \leq 1$, $0 \leq x \leq 0.2$): An Unexplored and Highly Efficient Electrocatalyst for the Oxygen Evolution Reaction. *ACS Applied Energy Materials*, *6*(3), pp.1308-1320.
12. Kuznetsov, D.A., Han, B., Yu, Y., Rao, R.R., Hwang, J., Román-Leshkov, Y. and Shao-Horn, Y., 2018. Tuning redox transitions via inductive effect in metal oxides and complexes, and implications in oxygen electrocatalysis. *Joule*, *2*(2), pp.225-244.
13. Bera, K., Karmakar, A., Karthick, K., Sankar, S.S., Kumaravel, S., Madhu, R. and Kundu, S., 2021. Enhancement of the OER kinetics of the less-explored α-MnO_2 via nickel doping approaches in alkaline medium. *Inorganic Chemistry*, *60*(24), pp.19429-19439.
14. Tang, L., Zhang, W., Lin, D., Ren, Y., Zheng, H., Luo, Q., Wei, L., Liu, H., Chen, J. and Tang, K., 2020. The hexagonal perovskite $Ba_{0.5}Sr_{0.5}Co_{0.8}Fe_{0.2}O_{3-\delta}$ as an efficient electrocatalyst for the oxygen evolution reaction. *Inorganic Chemistry Frontiers*, *7*(22), pp.4488-4497.
15. Fernandes, J.D., Melo, D.M.D.A., Zinner, L.B., Salustiano, C.D.M., Silva, Z.R., Martinelli, A.E., Cerqueira, M., Junior, C.A., Longo, E. and Bernardi, M.I.B., 2002. Low-temperature synthesis of single-phase crystalline $LaNiO_3$ perovskite via Pechini method. *Materials Letters*, *53*(1-2), pp.122-125.
16. Castro-Garcıa, S., Castro-Couceiro, A., Senarıs-Rodrıguez, M.A., Soulette, F. and Julien, C., 2003. Influence of aluminum doping on the properties of $LiCoO_2$ and $LiNi_{0.5}Co_{0.5}O_2$ oxides. *Solid State Ionics*, *156*(1-2), pp.15-26.
17. Ohzuku, T., Ueda, A., Nagayama, M., Iwakoshi, Y. and Komori, H., 1993. Comparative study of $LiCoO_2$, $LiNi_{1/2}Co_{1/2}O_2$ and $LiNiO_2$ for 4volt secondary lithium cells. *Electrochimica Acta*, *38*(9), pp.1159-1167.
18. Guilmard, M., Rougier, A., Grüne, M., Croguennec, L. and Delmas, C., 2003. Effects of aluminum on the structural and electrochemical properties of $LiNiO_2$. *Journal of Power Sources*, *115*(2), pp.305-314.
19. Vegard, L., Dale, H., 1928. Tests on mixed crystals and alloys. Z Krystallogr **1928**, 67(1), pp.148-162.
20. Joint Committee on Powder Diffraction Standards, File no. 074-0919.
21. Jones, C.D.W., Rossen, E. and Dahn, J.R., 1994. Structure and electrochemistry of $Li_xCr_yCo_{1-y}O_2$. *Solid State Ionics*, *68*(1-2), pp.65-69.
22. Shannon, R. D., 1976. *Actu Crystallogr. Sect. A,* 32, p.751.

23. Li, K. and Xue, D., 2006. Estimation of electronegativity values of elements in different valence states. *The Journal of Physical Chemistry A*, *110*(39), pp.11332-11337.
24. Feng, G.X., Li, L.F., Liu, J.Y., Liu, N., Li, H., Yang, X.Q., Huang, X.J., Chen, L.Q., Nam, K.W. and Yoon, W.S., 2009. Enhanced electrochemical lithium storage activity of $LiCrO_2$ by size effect. *Journal of Materials Chemistry*, *19*(19), pp.2993-2998.
25. Kalyani, P. and Kalaiselvi, N., 2005. Various aspects of $LiNiO_2$ chemistry: A review. *Science and Technology of Advanced Materials*, *6*(6), p.689.
26. Weckhuysen, B.M., Wachs, I.E. and Schoonheydt, R.A., 1996. Surface chemistry and spectroscopy of chromium in inorganic oxides. *Chemical Reviews*, *96*(8), pp.3327-3350.
27. Taha, T.A. and El-Molla, M.M., 2020. Green simple preparation of $LiNiO_2$ nanopowder for lithium ion battery. *Journal of Materials Research and Technology*, *9*(4), pp.7955-7960.
28. Anantharaj, S., Reddy, P.N. and Kundu, S., 2017. Core-oxidized amorphous cobalt phosphide nanostructures: an advanced and highly efficient oxygen evolution catalyst. *Inorganic Chemistry*, *56*(3), pp.1742-1756.
29. Lu, Z. and Dahn, J.R., 2002. Structure and electrochemistry of layered $Li[Cr_xLi_{(1/3-x/3)}Mn_{(2/3-2x/3)}]O_2$. *Journal of the Electrochemical Society*, *149*(11), p.A1454.
30. McCrory, C.C., Jung, S., Ferrer, I.M., Chatman, S.M., Peters, J.C. and Jaramillo, T.F., 2015. Benchmarking hydrogen evolving reaction and oxygen evolving reaction electrocatalysts for solar water splitting devices. *Journal of the American Chemical Society*, *137*(13), pp.4347-4357.